E-21-603

RESEARCH ON ALGaAs/GaAs INTERFACES IN GaAs SOLAR CELLS

A. Rohatgi and S. A. Ringel

Draft of Final Report for the Period

October 28, 1986 - February 28, 1988

Sandia National Laboratories

Contract No. 02-2255

GEORGIA INSTITUTE OF TECHNOLOGY
School of Electrical Engineering
Atlanta, GA 30332

TABLE OF CONTENTS

LIST OF FIGURES

LIST OF TABLES

1. INTRODUCTION

GaAs solar cells have been fabricated with efficiencies of 22% at one-sun and 26% under concentration, which are comparable to the best silicon cell efficiencies reported. However, very little is understood about the internal recombination mechanisms in III-V solar cells. For instance, peak internal quantum efficiencies in the best GaAs cells are only around 95% and decrease in the short wavelength part of the spectrum. High efficiency silicon cells have demonstrated internal quantum efficiencies near 100% over the entire useable spectrum. Identification of the internal recombination mechanisms in GaAs cells is necessary for further improvements in GaAs technology.

The objective of this research is to improve the basic understanding of internal loss mechanisms in GaAs solar cells, particularly their origin and ultimate influence on design criteria. The development of characterization techniques coupled with computer modeling was found essential to achieve the goal. A methodology consisting of electrical characterization, nondestructive defect profiling (SPAS), and computer modeling which allows the determination of internal loss mechanisms in an MOCVD grown GaAs p-n heteroface solar cell is presented. Parameters of particular interest are minority carrier lifetimes, bulk and interfacial recombination velocities, and deep levels. The cell performance is evaluated on the basis of these internal recombination parameters through extensive computer modeling. Device modeling is also used to show how a complete understanding of lifetime limiting mechanisms in GaAs coupled with clever cell design can result in cell efficiencies in excess of 25%.

2. TECHNICAL PROGRESS

2.1 Characterization, Modeling, and Optimization of High Efficiency GaAs Solar Cells

2.11 Introduction

As the conversion efficiencies of GaAs solar cells continue to increase, the ability to detect, analyze, and assess the importance of defects and other lifetime limiting mechanisms become critical to advance cell performance further. Most research to date has been devoted to the study of topics such as recombination centers in bulk GaAs [1,2] and at surfaces and interfaces using specialized test structures in which the interplay of interfacial effects with bulk properties such as minority carrier lifetime is not obvious [3-5]. Hence it is important to develop measurement techniques in conjunction with device modeling to separate those material parameters that dictate the performance of solar cells and other GaAs devices in which the carrier transport mechanisms are not well understood. Recently, a few attempts have been made to address this issue for GaAs solar cells [6-8].

This paper presents a combination of an electronic characterization methodology and device modeling to improve solar cell design by detecting and evaluating important material parameters such as lifetime, interface recombination velocity, and deep levels within a state-of-the-art MOCVD grown GaAs p-n heteroface solar cell. First, a number of standard semiconductor characterization techniques, such as DLTS (Deep Level Transient Spectroscopy) and dark I-V (current-voltage) and I-V-T were used to determine the carrier recombination and generation lifetimes separately. Then dopant profile and depth-

resolved surface photovoltage measurements were performed with the help of an electrochemical etching profiler to provide necessary inputs to the device modeling programs used in this investigation. A combination of a one dimensional computer model and the experimental data obtained through the above techniques was used to reveal the variation in the effective recombination velocity (S_e) throughout the device. S_e is indicative of net recombination anywhere within the device and can be used to guide the optimization of high efficiency cell design. A second device modeling program (PC-1D) was used to calculate cell parameters J_{sc}, V_{oc}, and efficiency along with the spectral response of the cell. The calculated values were correlated with the measured cell data to assess the accuracy of the characterization methodology to analyze the lifetime limiting mechanisms in the bulk and interfaces of GaAs structures. Finally, improved understanding of the loss mechanisms coupled with device modeling was used to provide guidelines for attaining GaAs cell efficiencies approaching 25% under AM1.5 conditions.

2.12 Experimental Methods

2.12(a) Device Structure

Figure 1 shows the device structure of the MOCVD grown GaAs heteroface solar cell used in this study, along with the measured cell data. The GaAs layers were grown at 700°C using trimethyl gallium and arsine as reactants. The AlGaAs was grown at 800°C using trimethyl aluminum for the Al source. The mole fraction of Al in the AlGaAs window layer was 0.90. Zn and Si were the p-type and n-type dopants, respectively, used throughout the structure.

For DLTS, I-V and I-V-T measurements, 50 mil diameter mesa dots were formed by evaporating Au/Zn ohmic contacts on the structure. The back surface

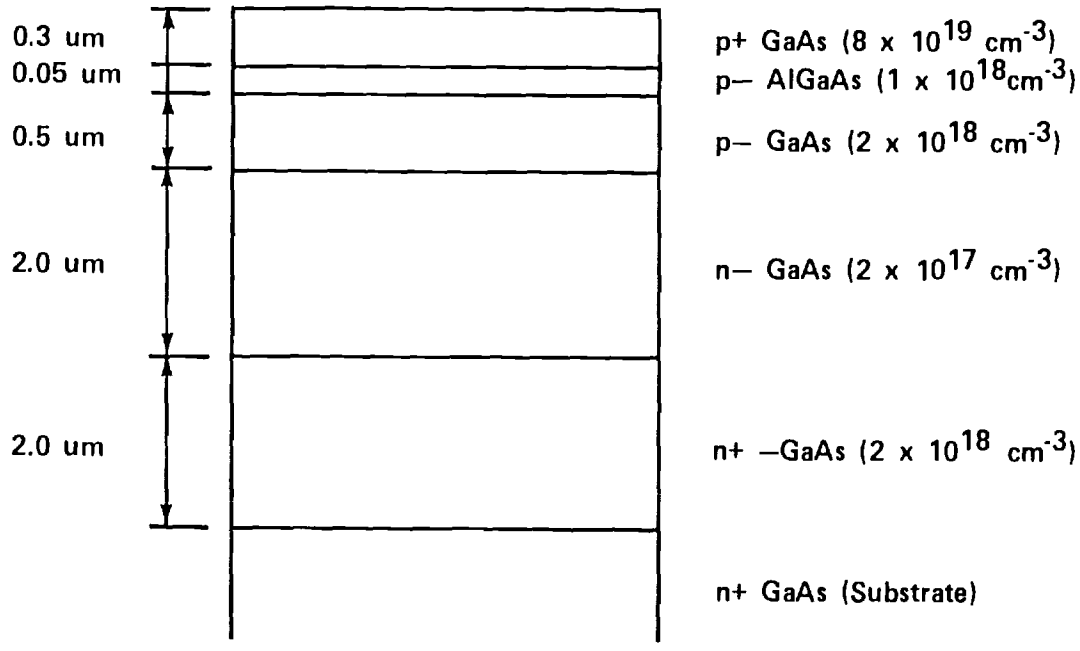

GaAs solar cell structure used in these experiments

V_{oc} = 1.013V J_{sc} = 24.5 mA/cm^2

F.F. = 0.867 Eff = 21.2%

Figure 1. Device structure and measured cell data of the MOCVD GaAs heteroface cell used in this study.

was covered with evaporated Au/Zn ohmic contacts to facilitate the electrical measurements.

2.12(b) Depth-Resolved SPV/C-V Measurements

Attempts were made to determine the carrier concentration profile and the spatial variation in the electro-optical response of the cell using a depth-resolved C-V and surface photovoltage (SPV) measurement. Both these measurements were performed in an automated electrochemical etching profiler in which an electrolyte is used to perform precise step-by-step etching coupled with I-V, C-V, and SPV measurements after each step [9]. A Schottky barrier formed between the electrolyte and the semiconductor facilitates both C-V and SPV measurements. The doping concentration is found from the C-V data at each depth. SPV measurements were performed in the wavelength range of 400 to 900 nm to accomodate both the GaAs and AlGaAs absorption edges. The SPV signal is measured at the surface under open circuit conditions to avoid electrochemical etching or deposition during the measurement. The choice of electrolyte is dictated by the properties of the semiconductor. For this study, a solution of 0.2 M NaOH + 0.1M EDTA (ethylenediamminetetraacetic acid) was found to be an adequate electrolyte for Schottky barrier formation and electrochemical etching and showed no signs of surface degradation.

2.12(c) DLTS Studies

A combination of DLTS and I-V-T measurements was used to determine the trap which controls the leakage current of the solar cell. The DLTS technique reveals all the detectable traps, regardless of their influence on the leakage current. DLTS measurements were made using an automated wafer analyzer system

which obtains data via a modified lock-in amplifier type DLTS setup. Nonuniformity in deep level distribution near the p-n junction of the solar cell was investigated by varying the steady reverse bias level from -5 volts to -1 volt but keeping the sum of the reverse bias and forward bias pulse height constant at -0.5 volts. In this way, the edge of the depletion region is steadily stepped toward the metallurgical junction as the reverse bias is decreased and a spatial trap profile of the depletion region is obtained. DLTS measurements were also performed in a forward bias mode (the sum of the steady reverse bias and the injection pulse height > the built-in voltage of the p-n junction) to detect both majority and minority carrier traps in the depletion region. It should be noted that the detection limit of our DLTS set-up is about 0.01% of the background doping concentration and hence defects with concentrations of less than 2×10^{13} cm^{-3} in the base region will not be detected.

2.12(d) I-V-T Analysis

The I-V-T technique, in contrast to DLTS, identifies only the activation energy of that deep level which limits the reverse leakage current as well as the generation/recombination lifetimes associated with it [10,11]. In addition, it does not suffer from the same doping dependent detection limit as DLTS, allowing information to be extracted from heavily doped device structures provided the trap is the dominant source of leakage. The carriers decay back to their equilibrium concentration by recombining at the deep level after an injection process. The generation lifetime associated with a deep level, τ_g, is the inverse of the decay process and becomes important where carrier concentration is low, such as the depletion region of a p-n junction.

The method is based on the assumption that the total reverse leakage current, J_o, is dominated by the space charge generation current, J_{o2}, and the diffusion component, J_{o1}, can be neglected under reverse bias. This is routinely observed in GaAs. From SRH (Schockly-Read-Hall) theory, the total carrier recombination rate, R, under steady state conditions is given by

$$R = \frac{np - n_i^2}{\tau_{po}(n + n_1) + \tau_{no}(p + p_1)} \tag{1}$$

where

$$\tau_{po} = (\sigma_p N_T v_{TH})^{-1} \tag{2}$$

$$\tau_{no} = (\sigma_n N_T v_{TH})^{-1} \tag{3}$$

$$n_1 = n_i \exp[\frac{(E_t - E_i)}{kT}] \tag{4}$$

$$p_1 = n_i \exp[\frac{-(E_t - E_i)}{kT}] \tag{5}$$

Under reverse bias conditions the excess carrier concentration in the space charge region can be neglected so that equation (1) reduces to

$$R = -n_i/\tau_g \tag{6}$$

with

$$\tau_g = \tau_{po}\exp[\frac{(E_t - E_i)}{kT}] + \tau_{no}\exp[\frac{-(E_t - E_i)}{kT}] \tag{7}$$

where E_t is the energy level of the recombination center within the bandgap and E_i is the position of the intrinsic Fermi level. If the capture cross section for holes (σ_p) and electrons (σ_n) are comparable then τ_g reduces to

$$\tau_g = \tau_{po} \exp\left[\frac{(E_t - E_i)}{kT}\right] \qquad \text{for } E_t > E_i \tag{8}$$

or

$$\tau_g = \tau_{no} \exp\left[\frac{-(E_t - E_i)}{kT}\right] \qquad \text{fpr } E_t < E_i \tag{9}$$

but more generally,

$$\tau_g = \tau_r \exp\left[\frac{(E_t - E_i)}{kT}\right] \tag{10}$$

Using the definition of leakage current in a reverse-biased diode [12] and recalling the assumption which neglects the J_{o1} component of J_o,

$$J_{rev} = J_{o2} = \frac{qn_iW}{\tau_g} \tag{11}$$

where W is the width of the depletion region, then

$$J_{o2} \propto \exp\left[\frac{-(E_t - E_v)}{kT}\right] \qquad \text{for } E_t > E_i \tag{12}$$

or

$$J_{o2} \propto \exp\left[\frac{-(E_c - E_t)}{kT}\right] \qquad \text{for } E_t < E_i \tag{13}$$

Hence, the activation energy of the generation center which controls the leakage current can be determined from the slope of the $\ln(J_{o2})$ vs. 1000/T plot under constant applied reverse bias. It is important to note that the I-V-T method gives an activation energy of the trap which controls the leakage current but it does reveal the band edge with respect to which that activation energy is measured, unless the trap location is known. Therefore, this method

must be supplemented by other measurements such as DLTS which gives all the traps present but does not reveal which one controls the leakage current.

2.12(e) Transformed I-V Analysis

The I-V characteristic of the mesa diode structure was measured in the dark and analyzed using an automated setup to separate the resistance, bulk and junction region effects. The I-V characteristic of a solar cell is a composite of two exponential functions including series and shunt resistance effects. The transformed I-V program first measures and subtracts the resistance effects from the measured data and then fits the rest to a double exponential equation given by

$$J = J_1 + J_2 = J_{o1}\left[\exp\left(\frac{qV}{kT}\right) - 1\right] + J_{o2}\left[\exp\left(\frac{qV}{nkT}\right) - 1\right] \qquad (14)$$

where J_{o1} and J_{o2} are the saturation current densities for the diffusion (n=1) and space charge generation (n) current components, respectively. The computer program fits the data and provides values of J_{o1} and J_{o2}.

2.13 Results and Discussion

The doping profile throughout the device structure, Figure 1, was confirmed by depth-resolved C-V measurements. Since the doping level in the AlGaAs window layer is similar to that of the emitter, the AlGaAs layer was not evident. Presence of the AlGaAs layer was confirmed by far infrared reflectance measurements which also revealed the mole fraction of Al to be 0.87, close to the target composition. The AlGaAs thickness was found to be 50 nm by reflectance measurements.

Spatial variations in the material properties were investigated by depth-resolved SPV measurements in an electrochemical profiler. Figure 2 shows photovoltage spectra taken at various etch depths. This data was not taken on the actual cell but on a piece adjacent to it, which has the p^+ GaAs cap layer intact. The initial (0.12-0.21 um) increase in the response with increasing etch depth is due to the successive removal of the heavily doped cap layer which has high absorption and recombination. The two humps at 560 nm and 720 nm are the characteristic response of the SPV optics. The etch depths at which these measurements were made are indicated in the figure. Both the overall shape and magnitude of SPV response are related to the properties of the material being probed. As we etch through the emitter region (0.21-0.42 um) the response gradually drops. This does not necessarily indicate defects or nonuniformity in the emitter region, but instead could be the result of enhanced competition from the p-n junction for the carriers generated within the emitter region. Notice that the overall open-circuit signal represents the spectrally resolved sum of the opposing photovoltages generated at the front electrolyte/GaAs Schottky barrier and at the p-n junction [9]. At present it is not known how to quantitatively account for the effect of the p-n junction influence on the measured response.

A qualitative picture of material uniformity can be obtained from spectrally resolved divisions of consecutive SPV spectra. Figure 3 shows a series of ratios taken while the device is being etched through the emitter. SPV ratio curve "a" indicates that a fraction of the carriers generated at longer wavelengths are either being lost to the p-n junction or to a defective layer near it since the ratio there is less than unity. The sign change in the SPV ratio curve "b" of Figure 3 taken just before the p-n interface, indicates

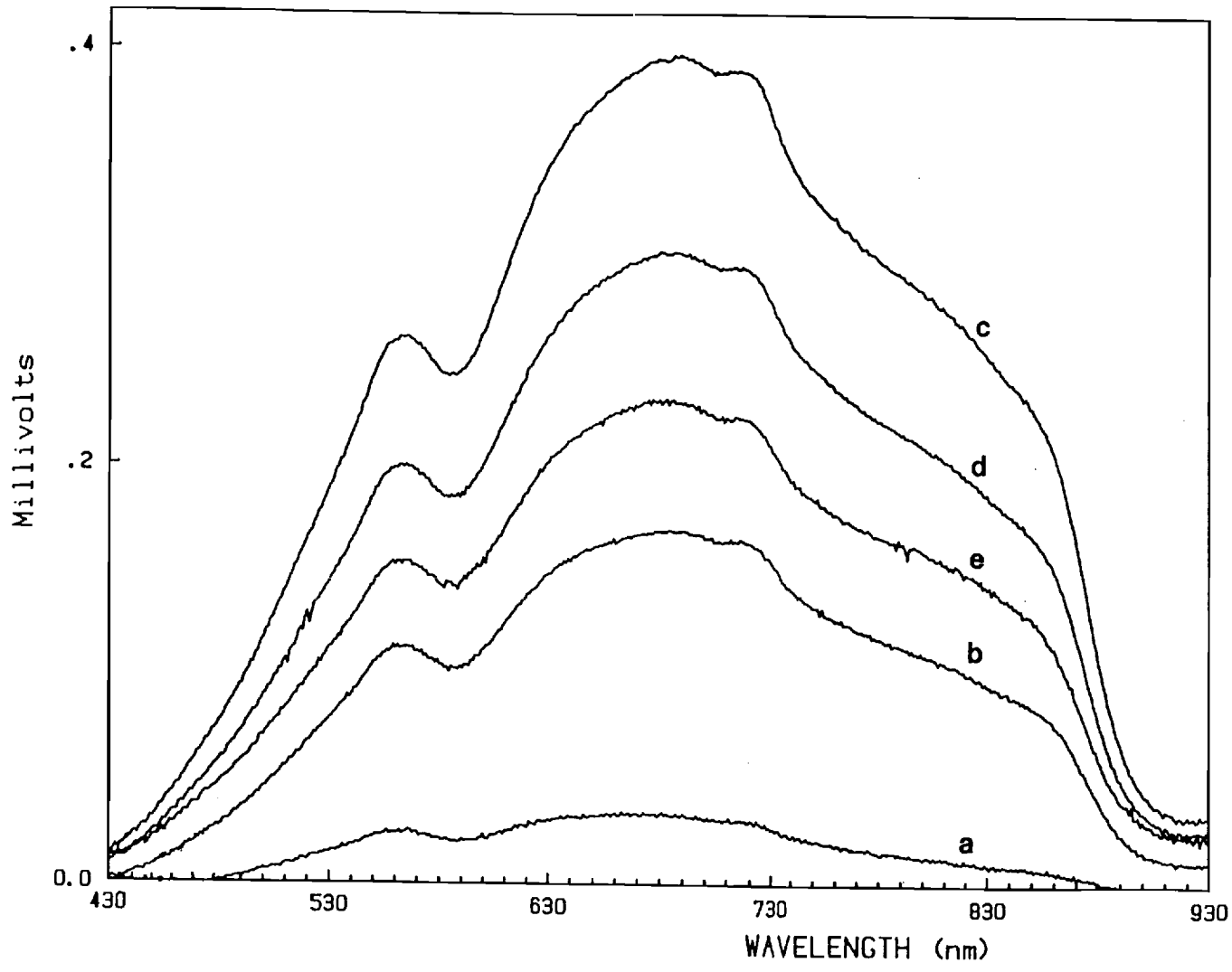

Figure 2. Variation of SPV response as the device is etched through. The measurements were taken at etch depths of (a) 0.12 um, (b) 0.17 um, (c) 0.21 um, (d) 0.3 um, and (e) 0.42 um.

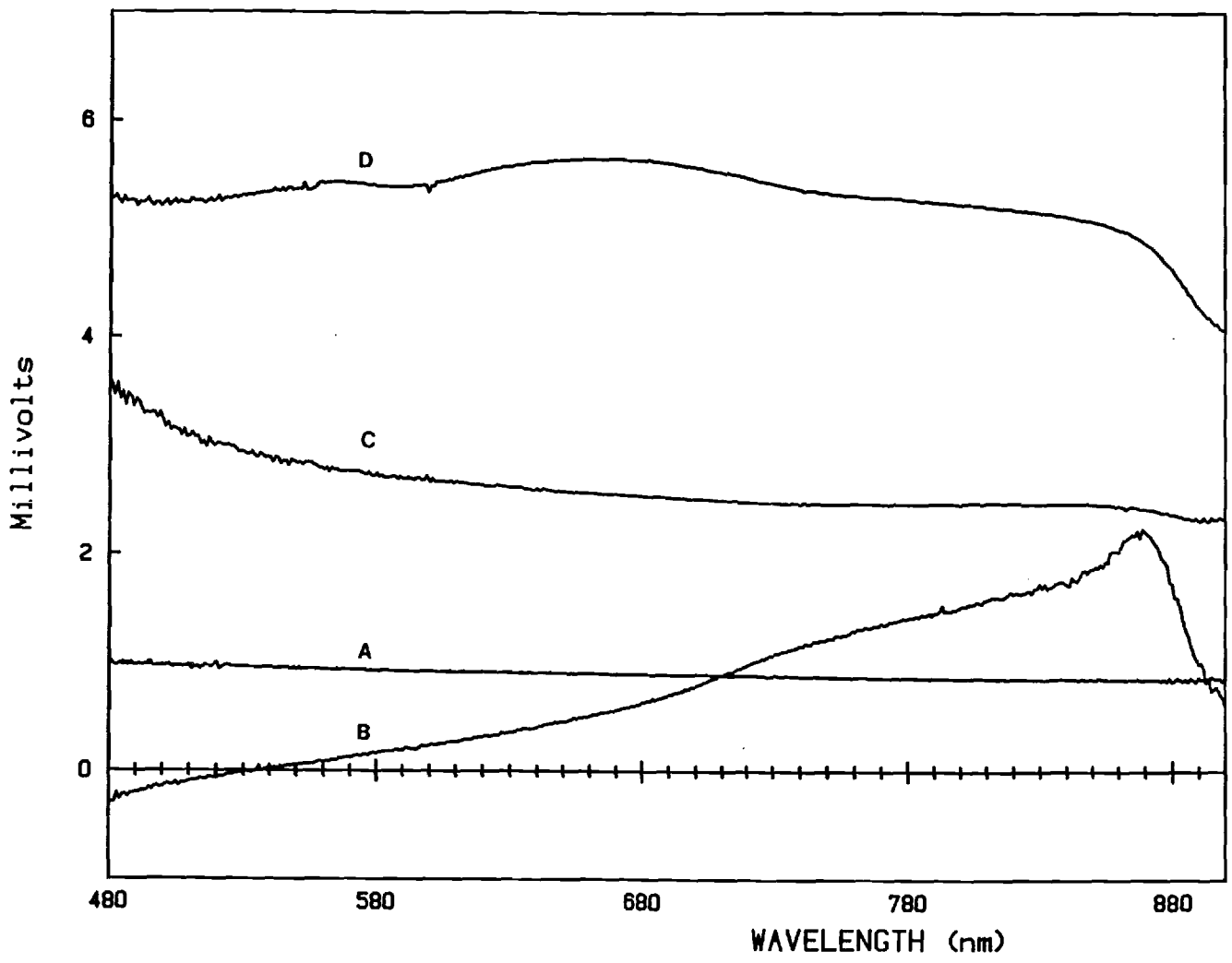

Figure 3. Ratios between SPV spectra taken at: (a) front of emitter; (b) just before p-n junction; (c) just after p-n junction; (d) 0.1 um after curve (c).

that for photons with wavelength greater than ~ 530 nm the p-n junction becomes the dominant carrier collecting junction. Up to this point, the effect of the presence of a defective region of material could be masked by the competition from the p-n junction. However, the SPV ratio curves"c" and "d", obtained by etching through the p-n junction and another slice 0.1 um later, respectively, do not suffer from this complication. The ratio curves c and d suggest that near the p-n junction, the material quality is improving in the base as we move away from the junction edge because the ratios are not only greater than one but gradually increase with depth, in spite of the constant base doping.

From the depth-resolved SPV measurements, it appears that the defect density may be increasing as we approach the p-n junction. To investigate this further, depth-resolved DLTS measurements were performed on the same wafer using the mesa structure described earlier. The DLTS primarily probes the n-base side of the p^+-n junction. Figure 4 shows that a deep level was detected only when the probed depletion region got close to the p-n interface. This minority carrier trap had an activation energy of E_v + 0.912 eV and a concentraton of 3.93 + $10^{14}cm^{-3}$. The fact that this level was not detected for wider depletion widths supports the nonuniform defect distribution seen by the SPV response near the p-n junction. The ln(J) vs T plot from the I-V-T measurement, Figure 5, gave an activation energy of E_a = 0.4523 eV for the J_{o2} component. Since the sum of the DLTS and I-V-T activation energies is close to the bandgap of GaAs (0.4523 + 0.912 = 1.36 eV), it is reasonable to conclude that the level detected by DLTS and I-V-T is the same and is also responsible for the excess leakage current.

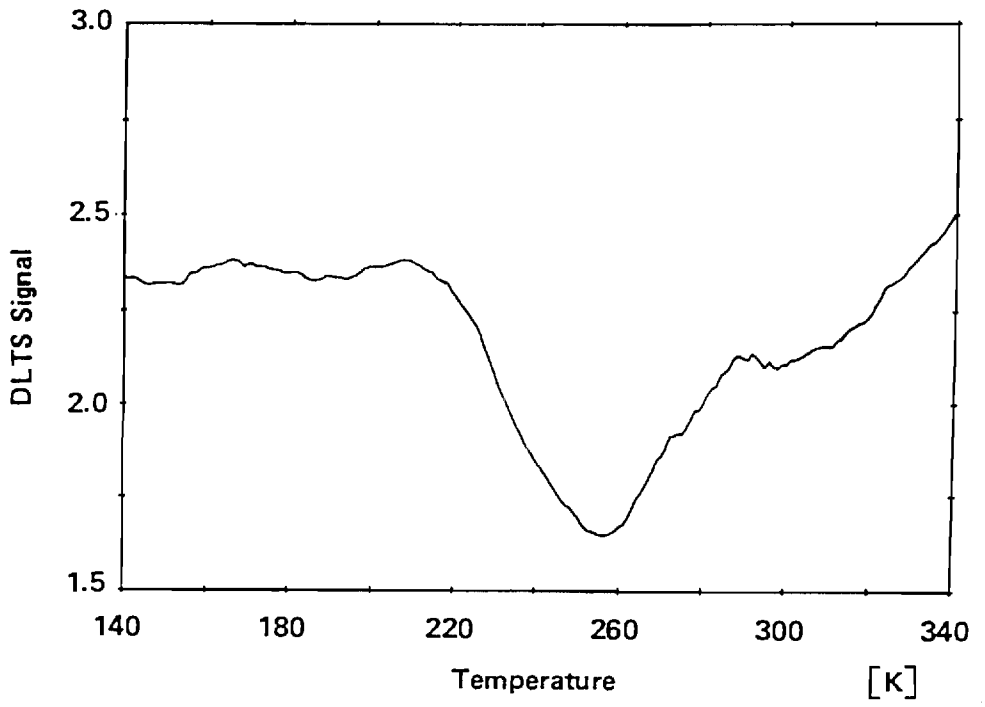

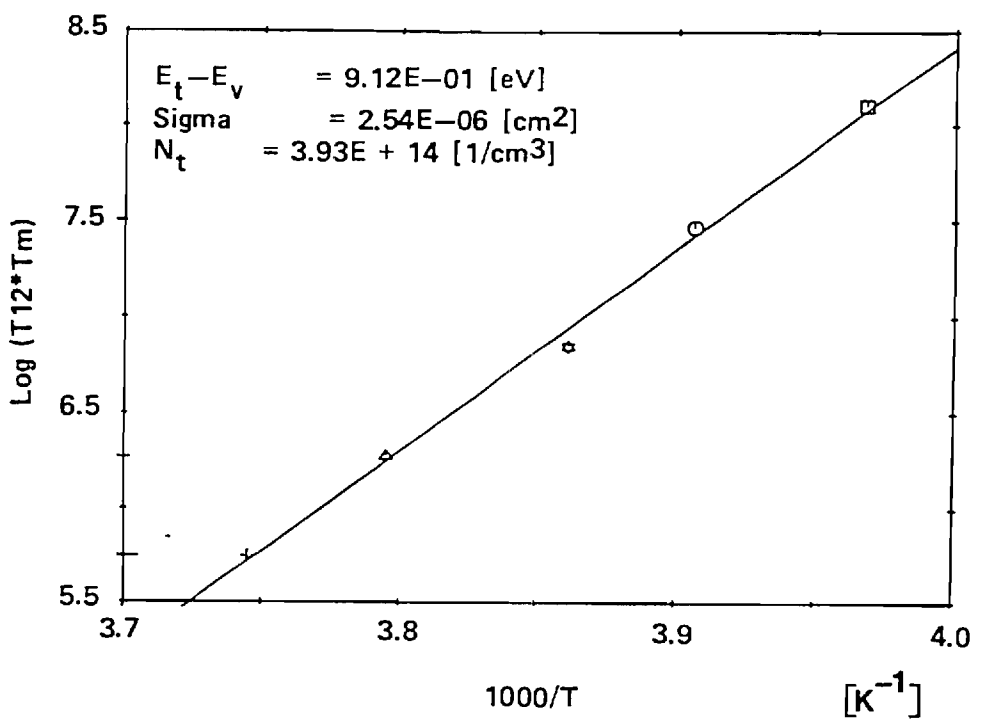

Figure 4. DLTS scan and activation energy plot indicating the presence of a hole trap in the n-type base depletion region.

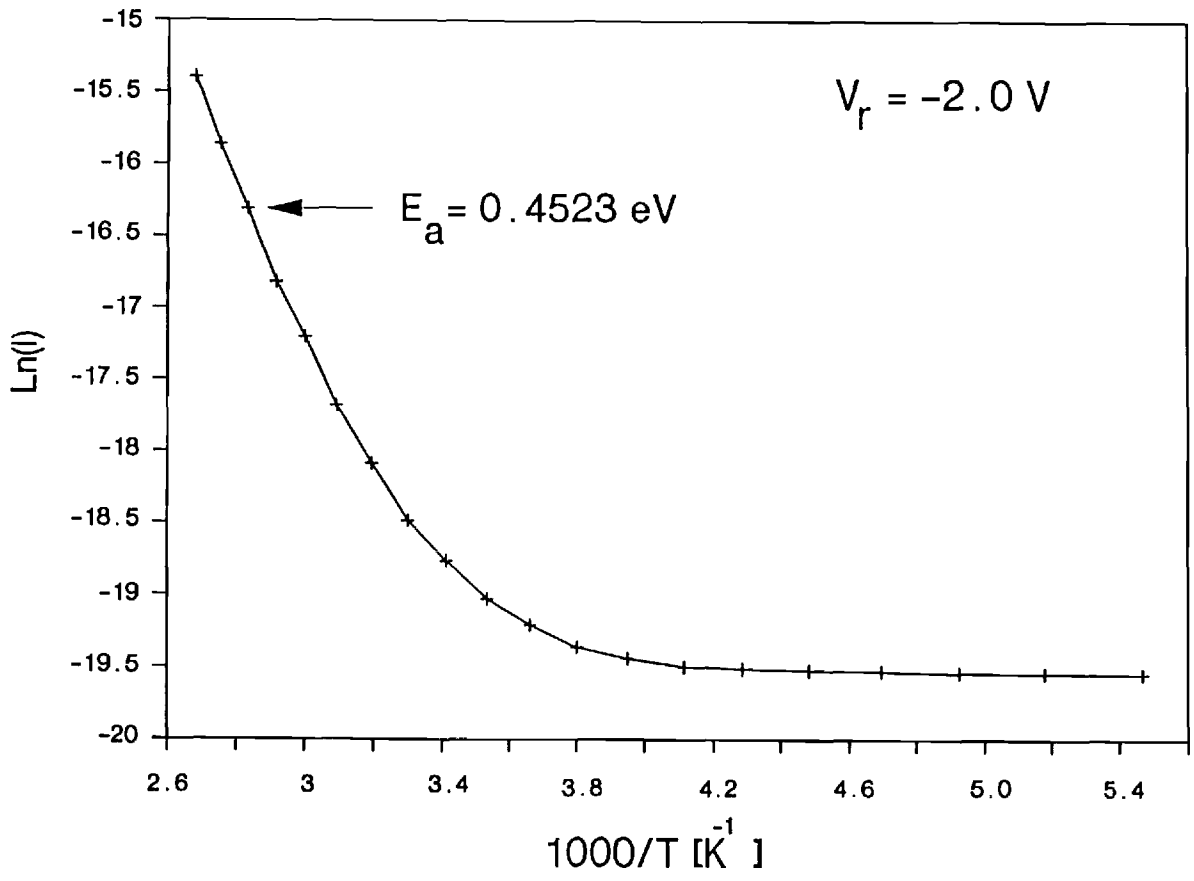

Figure 5. LN(J) vs. T plot measured at 2 volts constant reverse bias. Trap activation energy is shown in the figure.

While the DLTS and I-V-T measurements yield the characteristics of the space charge region, they offer no information about the bulk material properties. In order to assess the bulk properties the transformed I-V technique was used to separate the bulk and junction effects. Figure 6 shows the transformed I-V curve for this device at room temperature. J_{o1} and J_{o2} components were found to be 1.29 E - 19 A/cm^2 and 8.33 E - 11 A/cm^2, respectively, while the corresponding n-factors were 1.00 and 1.97, consistent with theory.

Even though the trap detected by I-V-T and DLTS could not be seen deeper in the base, the leakage current produced in the depletion region of this cell degrades the cell performance because the J_{o1} and J_{o2} components are nearly equal at the cell operating point (~1 volt), Figure 6. Since the J_{o2} component at the operating point represents the current that does not make it to the load, performance of this particular cell can be appreciably improved by eliminating the E_v + 0.912 eV trap.

2.14 Computer Modeling

To test the experimental data and the validity of the above analyses, the solar cell was modeled with the help of two computer programs, one of which calculates the cell parameters V_{oc}, J_{sc}, efficiency, and spectral response, and the other which calculates an effective recombination velocity anywhere within the structure.

The PC-1D model, described elsewhere (13), was used first to model the spectral response. A net base lifetime of 8 ns with a front surface recombination velocity of 1.25 E5 cm/s was required to obtain a good match between the model calculations and the experimental data, Figure 7. Back surface passivation was found to have negligible effect on the spectral response. The

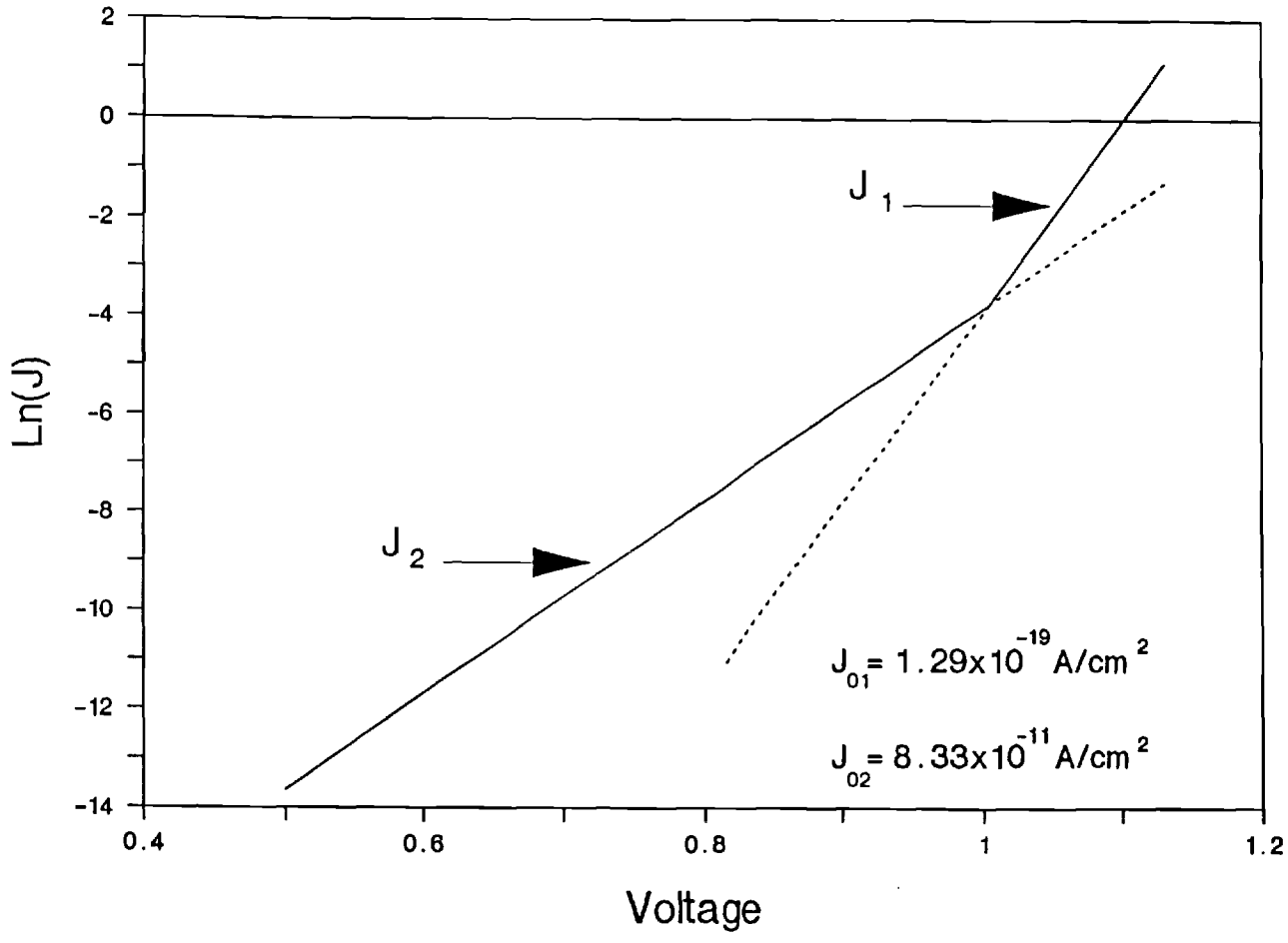

Figure 6. Transformed I-V characteristic for cell. J_1 (diffusion) and J_2 (space charge) current density components are indicated.

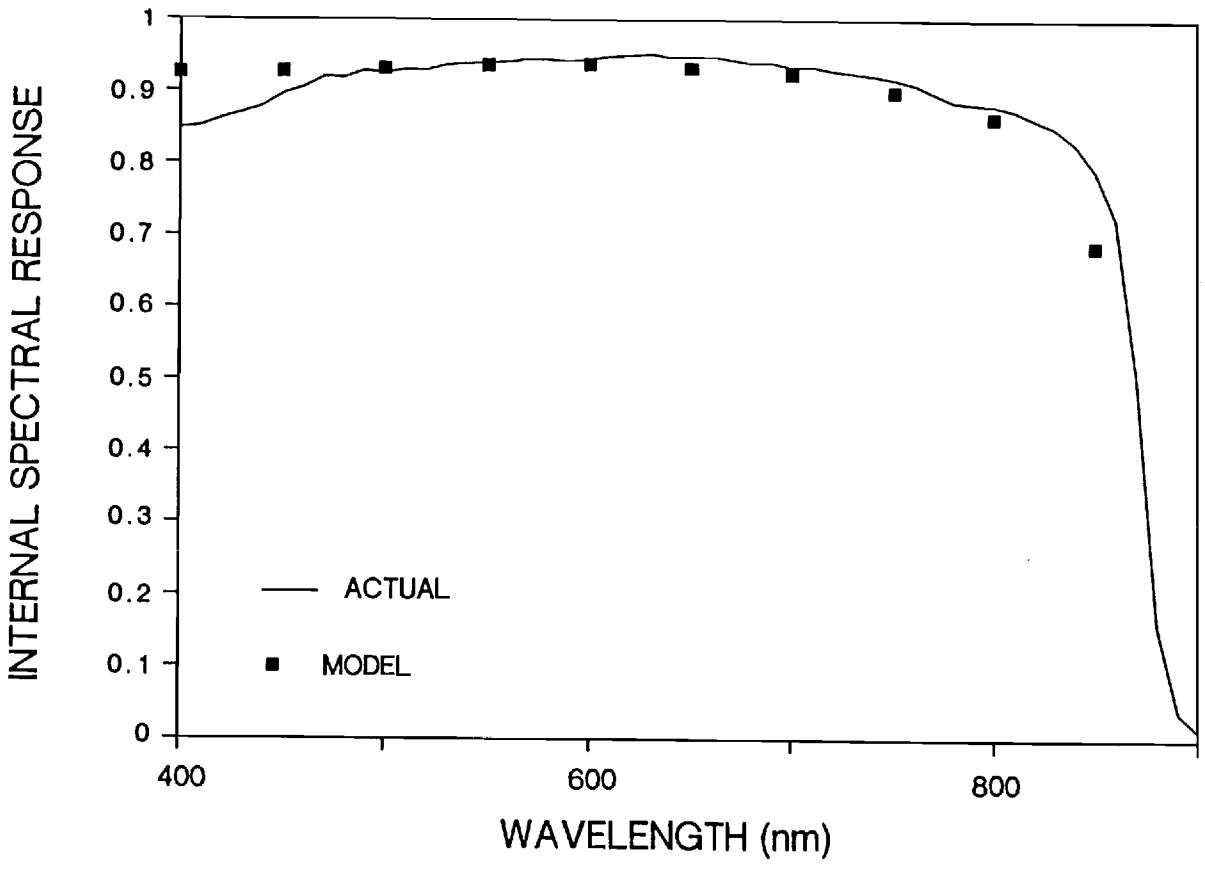

Figure 7. Comparison of actual spectral response (solid line) with modeled spectral response (blocks) as calculated from PC-1D for the given device structure.

emitter and buffer lifetimes were determined from the SRH lifetime in the base which was calculated from

$$\frac{1}{\tau} = \frac{1}{\tau_{srh}} + BN + CN^2 \tag{15}$$

where B is the radiative recombination coefficient and C is the Auger recombination coefficient for GaAs. Using B = 2.5 E - 11 cm^3 [14], C = 1.60 E - 29 cmI.^{6} [15], and τ_B = 8 ns in the base, we obtain τ_{srh} = 8.33 ns. Assuming defect dominated τ_{srh} to be constant throughout the device, equation (15) gave emitter and buffer lifetimes of 2.08 ns and 5.49 ns, respectively, by substituting the proper values for B and C in each region.

The numerical values of the spectral response, Figure 7, were found from the calculated J_{sc} and measured reflectivity as a function of wavelength using the AM1.5 energy content of the incident radiation. A shadow loss of 5% was used for the modeling. Figure 7 shows a good match between the calculated and measured values with only a slight difference in the short and long wavelengths. The lower measured response in the short wavelength, seen in Figure 7, can be attributed to absorption in the AlGaAs passivation layer which is not considered in the model. The AlGaAs acts to decrease the photon flux incident on the GaAs at the shorter wavelengths until the absorption edge of the AlGaAs at ~2 eV is reached. At long wavelengths (850 nm), the simulated response is somewhat lower than the actual probably because the increase in absorption coefficient due to doping near the band edge [16] is not included in the PC-1D model. This additional absorption allows more photons to be absorbed closer to the collecting junction and hence increase J_{sc} at these long wavelengths due to an increase in collection probability.

In order to test the estimated lifetime profile (τ_e, τ_b, τ_{buff}) and recombination velocities, an effective recombination velocity (S_e) model was used to calculate the reverse leakage current. S_e is a measure of the minority carrier losses in the various regions of the device which directly provides the reverse saturation current density (J_{o1}). This model, which is described in detail elsewhere for silicon cell design and analysis [17], includes the effects of bandgap narrowing, Auger and radiative recombination, and recombination at surfaces and interfaces. The internal recombination velocity S_e throughout the cell can be calculated using the front surface recombination velocity at the emitter/AlGaAs interface, FSRV, the back surface recombination velocity at the back of the buffer layer, BSRV, the diffusion length, doping profile, and cell dimensions as input parameters. Each region of the cell (buffer, base, and emitter) is subdivided into a number of elements, all of the same width. S_e is calculated iteratively from FSRV and BSRV until the p-n junction edge is reached on each side. The recombination velocity S_{e2} at one boundary of any element is calculated in terms of velocity S_{e1} at the other boundary by

$$S_{e2} = \frac{N_2}{N_1}\frac{D}{L}\left[\frac{S_{e1}\frac{D}{L} + \tanh(\frac{W}{L})}{1 + S_{e1}\frac{D}{L}\tanh(\frac{W}{L})}\right] \exp\left[\frac{\Delta E_{g2} - \Delta E_{g1}}{kT}\right] \tag{16}$$

where

W = element width

D,L = diffusion coefficient and diffusion length of minority carriers within the element

$N_{1,2}$ = doping densities at boundaries of element

ΔE_{g1}, ΔE_{g2} = bandgap narrowing due to doping densities N_1 and N_2.

The base and emitter components of the leakage current can then be determined from

$$J_{0B} = \frac{qn_i^2}{N_D} \cdot S_{ejb} \tag{17}$$

and

$$J_{0E} = \frac{qn_i^2}{N_A} \cdot S_{eje} \tag{18}$$

where S_{ejb} and S_{eje} are the recombination velocities at the base edge and emitter edge of the p-n junction, respectively.

Figure 8 shows a plot of S_e versus depth for the GaAs heteroface cell for various values of FSRV and BSRV which support the spectral response conclusion that back-surface passivation has little or no effect on J_{0B} in this cell. The model calculations reveal that recombination velocity at the base side of the p-n junction is pinned so that $J_{0B} = \sim 0.85 + 10^{-19}$ A/cm^2 for all values of back surface recombination velocity. For FSRV = 1.25 X 10^5cm/s and τ_e = 2.08 ns, which gave the best match for the spectral response, the S_e-model gives J_{0E} = 0.55 X 10^{-19}A/cm^2 so that the simulated $J_{o1} = J_{0E}$ X J_{0B} = 1.40 + 10^{-19} A/cm^2. This is in good agreement with the measured J_{o1} of 1.29 X 10^{-19} A/cm^2. This supports the selection of FSRV and lifetime for the simulated spectral response and indicates that J_{o1} or V_{oc} of this cell is limited by both the base and emitter with the emitter contributing ~ 33% of J_{o1}.

A few more revealing observations can be made from Figure 8. Contrary to the back surface, front surface passivation is critical for this cell because an FSRV of 1 X 10^7cm/s, which is typical of the free GaAs surface, results in a large increase in J_{0E} and hence a lower V_{oc}. However, the AlGaAs passivation needs to limit FSRV only to ~1 X 10^4cm/s since in this cell FSRV

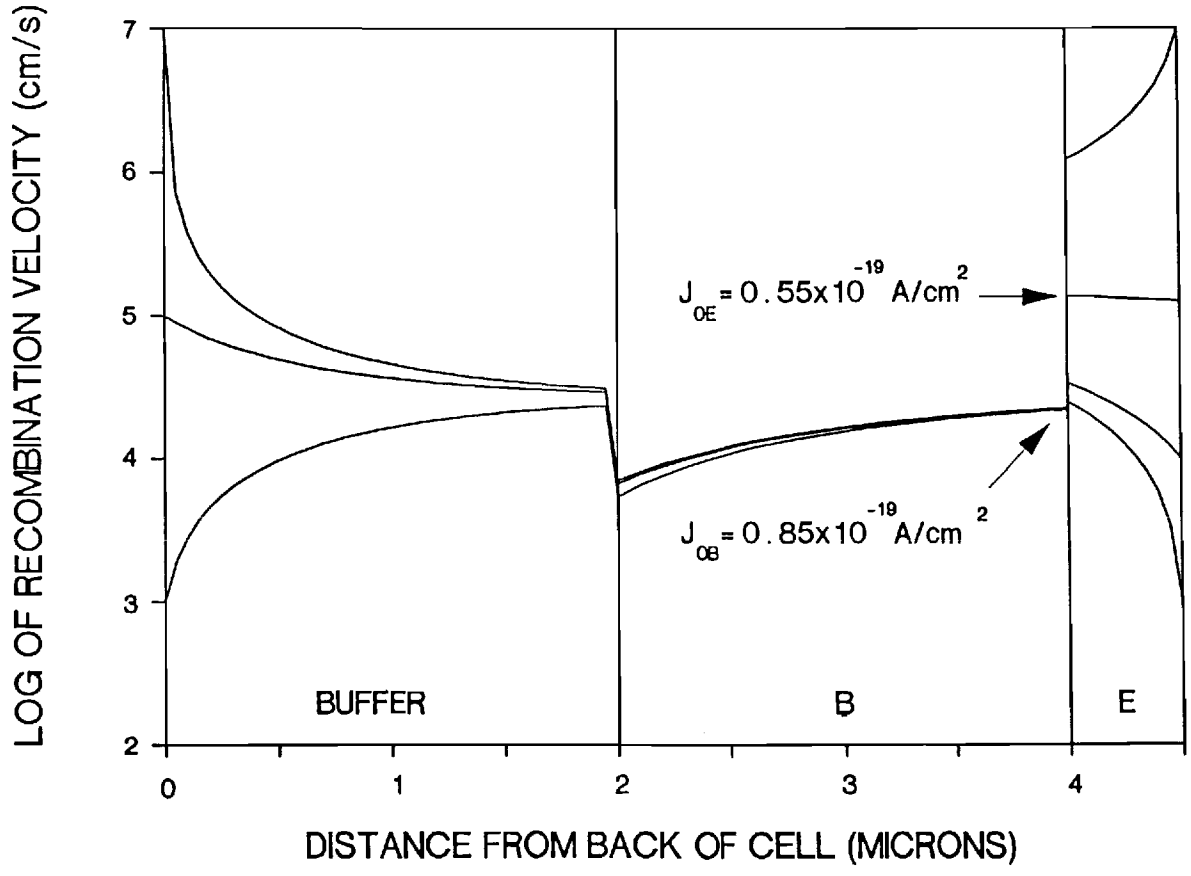

Figure 8. Plot of effective recombination velocity, S_e, for various values of front and back surface recombination velocities. Emitter and base leakage current components are indicated for the cell-matching S_e plot.

below this value has very little impact on S_{eje} or J_{0E} as seen in Figure 8. Note also from this figure that the design rule for the emitter changes with the magnitude of FSRV. For devices with any reasonable amount of surface passivation a lower J_{0E} is accomplished by thinning the emitter, but for unpassivated surfaces, emitter thinning would actually increase J_{0E}. Thus, the AlGaAs passivation is most critical for thin emitters.

As a final confirmation of the lifetime profile and the S values derived above, the cell J_{sc}, V_{oc}, and efficiency were calculated using PC-ID. Table 1 shows a very good agreement between the measured and modeled values confirming the validity of the above procedure. Having established the match, the PC-1D model was used to provide guidelines for improving the efficiency of this cell and to optimize the p-n heteroface cell design. Model calculations in Table 1 show that a significant improvement in cell efficiency (23%) can be realized by properly passivating the front surface of this cell so that the FSRV = 1 + 10^4cm/s. Only a slight improvement is found by back surface passivation for the lifetime profile of this device structure. However, if the effective base lifetime can be improved to 15 ns the efficiency of this cell can reach ~24.17% with passivated front and back surfaces. This improvement is clearly understood upon inspection of Figure 9 which shows that longer lifetimes decrease the magnitudes of S_{eje} and S_{ejb} resulting in higher V_{oc}, in additon to raising J_{sc} via reduced recombination throughout the device. Further gain in efficiency can be obtained by optimizing the thickness and doping profile of the device. Since in n-type GaAs the net lifetime is dominated by defects up to a doping level of ~1 X 10^{18} cm^{-3} [7], an efficiency of ~24.40% can be obtained simply by changing the base doping to 5 X $10^{17}cm^{-3}$ and the buffer doping to 2.5 X $10^{18}cm^{-3}$. These doping levels represent the

Table 1: Guideline for cell optimization using PC-1D and effective recombination velocity modeling. Actual cell data and best match are shown. Cells 6 and 7 (starred entries) are thinnned base and buffer structures.

cell ID	N_d (cm^{-3})	N_a (cm^{-3})	N_b (cm^{-3})	FSRV (cm/s)	BSRV (cm/s)	T_b (ns)	V_{oc} (Volts)	J_{sc} (A/cm^2)	Eff
actual	2×10^{17}	2×10^{18}	2×10^{18}				1.013	24.5	21.2
match	2×10^{17}	2×10^{18}	2×10^{18}	1.25E5	1.0E6	8	1.01	24.56	21.39
1	2×10^{17}	2×10^{18}	2×10^{18}	1.0E4	1.0E6	8	1.016	26.59	23.02
2	2×10^{17}	2×10^{18}	2×10^{18}	1.0E4	1.0E4	8	1.017	26.71	23.13
3	2×10^{17}	2×10^{18}	2×10^{18}	1.0E4	1.0E4	15	1.032	27.11	24.17
4	5×10^{17}	2×10^{18}	2.5E18	1.0E4	1.0E4	15	1.048	26.83	24.40
5	5×10^{17}	2×10^{18}	2.5E18	1.0E4	1.0E4	20	1.054	26.95	24.76
6*	6×10^{17}	2×10^{18}	2.5E18	1.0E4	1.0E3	15	1.055	27.04	24.74
7*	6×10^{17}	2×10^{18}	2.5E18	1.0E4	1.0E3	20	1.0596	27.10	25.04

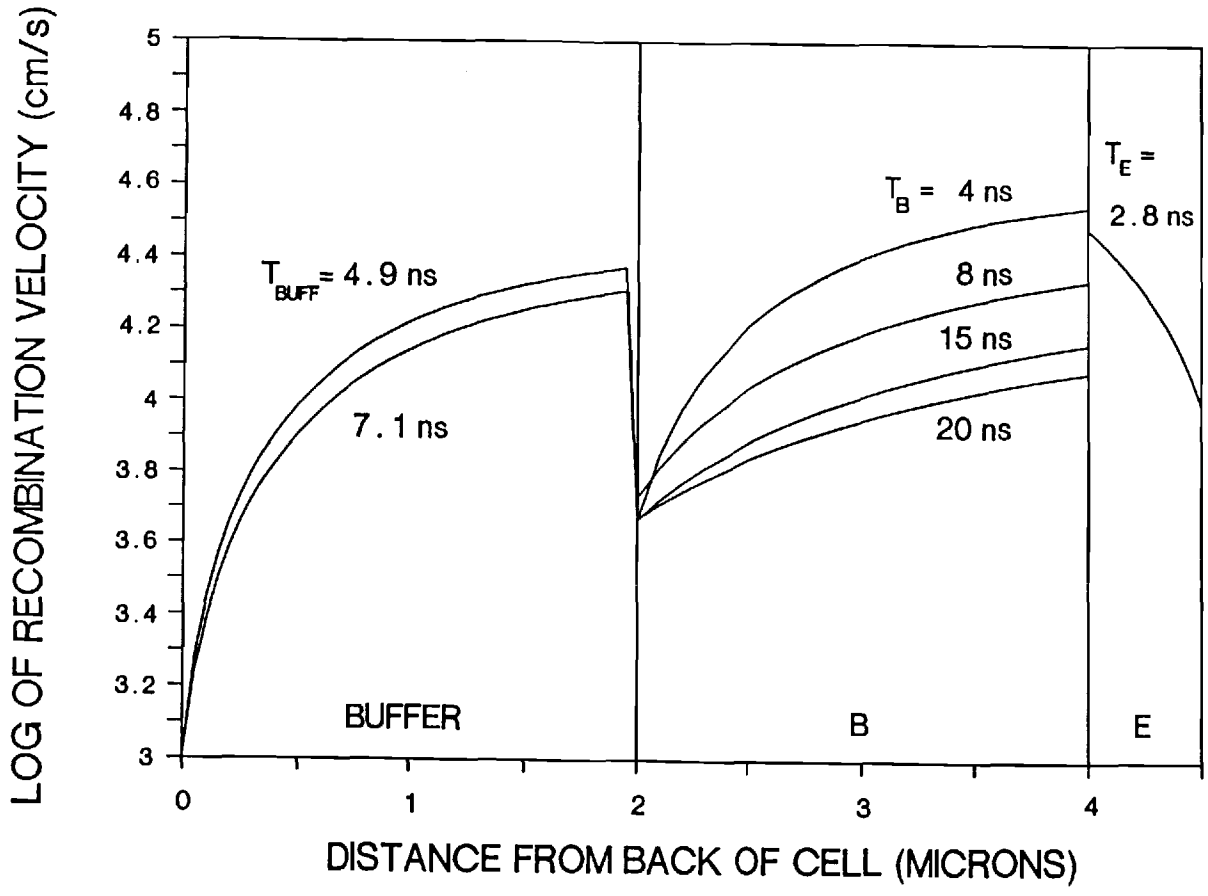

Figure 9. Plot of effective recombination velocity, S_e, showing the influence of minority carrier lifetime on recombination throughout the device. The net lifetimes in each layer are indicated.

optimum trade-off between an increase in V_{oc} due to the heavier base doping and a decrease in J_{sc} resulting from higher S_e in the base due to a reduced doping discontinuity (N_1/N_2) at the buffer/base interface. It should be recognized that these calculations are easily deduced from S_e-plots which signify the importance of such analysis. The cell efficiency tends to saturate near the 24.40% level unless the base material quality is improved further. Table 1 shows an efficiency of 24.76% can be obtained with a lifetime of 20 ns, which is still well below the intrinsic lifetime limit of GaAs at a doing level of 5 X $10^{17}cm^{-3}$. This represents the highest efficiency found for our simulations of this particular p-n heteroface structure.

Further optimization is possible only by modifying the device structure. Table 1 shows that a 24.74% efficient cell can be achieved with only a 15 ns base lifetime by thinning the base to 1.2 um. This improvement comes as a result of the trade-off between low S_e in the base and increased photon absorption in the buffer. For this device structure, it is necessary to have a passivated back surface and reasonable lifetime in the buffer. The doping and thickness of the base and buffer layers become critical to the performance of such a device since there exists a sensitive trade-off between greatly increased carrier collection in the thinned based due to reduced recombination in the base resulting from the proximity of the base/buffer interface to the collecting junction, and the amount of carriers generated in the buffer layer that do not make it to the p-n junction. The V_{oc} is greatly increased due to the lower S_{ejb} while the J_{sc} benefits from the higher collection efficiency of photogenerated carriers in the thin base. Model calculations in Table 1 indicate efficiencies as high as ~25.04% are possible for a device with a base width of 1.2 um, buffer thickness of 1.3 um, base doping of 6 X $10^{17}cm^{-3}$,

buffer doping of 2.5 X $10^{18}cm^{-3}$, base lifetime of 20 ns, FSRV = 1 X 10^4cm/s and BSRV = 1 X 10^3cm/s. It should be noted that the buffer thickness now becomes important since the effectiveness of the back surface passivation would be reduced if the buffer were too thick. In essence, the buffer here acts as part of a two-step base layer which suggests that further gains in efficiency can be realized by multi-step or even graded base regions.

2.2 Positron Annihilation Spectroscopy of AlGaAs/GaAs Interfaces in MOCVD-Grown GaAs Heterojunction Solar Cells

2.21 Introduction

A major objective in the characterization of heterojunction semiconductors grown via MOCVD, MBE, or PEVD is the development of techniques for probing defect and impurity distributions affecting the electrical response. Thus, methodologies can be developed for adjusting deposition parameters, layer thickness, and/or dopant density to enhance the electrical properties of the semiconductor. Furthermore, from a quality assurance viewpoint, it is desirable that techniques for characterizing the atomic defect and/or impurity structure of a semiconductor be non-contact (NC) and nondestructive (ND). One relatively new technique that satisfies the NC and ND constraints and is capable of profiling the defect density, detailing interfacial disorder, and detecting impurity complexes is Slow Positron Annihilation Spectroscopy (SPAS) [17-21].

By measuring the energy distribution of positron/electron annihilation events it is possible to probe a material's electron momentum distribution with a variable-energy positron beam. As a first order approximation, the intensity of the parabolic and Gaussian components of the annihilation energy

distribution can be related to the respective fractions of positrons annihilating with valence electrons and those annihilating with the more tightly bound core electrons. If a positron becomes spatially localized due to defect trapping or to strong space charge effects, the fraction of annihilation events with valence electrons will be altered relative to core electrons, thus narrowing or broadening the energy distribution curve.

A series of experiments was carried out to determine the potential applications of SPAS to heterojunction semiconductors by investigating the relative positron-sensitive defect profile for different MOCVD grown solar cell structures. Validation of any new microanalytical tool requires extensive comparisons with other more established techniques, wherever possible. The SPAS data has been subsequently compared to Surface Photo-Voltage (SPV), a destructive defect profiling technique, qualitative MOCVD growth variations, and band bending arguments.

2.22 Experiment

The MOCVD grown solar cell structures investigated are summarized in Table 2, in terms of layer function, material, semiconductor type, and dopant density. These devices were grown in a Spire MO-450 reactor using trimethyl gallium, trimethyl aluminum, and arsine as reactants. The dopants are Zn for p-type regions and Si for the n-type regions.

The variable-energy positron beam (0 - 100 keV) used for analysis of the heterojunction solar cells has been previously described elsewhere [24]. In brief, the system consists of a Na-22 positron source moderated by a tungsten crystal with efficiency 5×10^{-4} and focused magnetically to the target, all of which is under UHV conditions (10^{-10} Torr). At each incident energy,

TABLE 2. SOLAR CELL HETEROJUNCTION STRUCTURES

LAYER	MATERIAL	THICKNESS (um)	TYPE	DOPING (cm^3)
MOCVD Run #872				
Cap	GaAs	0.143	p^+	8.0×10^{19}
Window	AlGaAs	0.05	p^+	1.0×10^{18}
Emitter	GaAs	0.5	p	1.5×10^{18}
Base	GaAs	2.0	n	2.0×10^{17}
Buffer	GaAs	2.0	n	2.0×10^{18}
Substrate	GaAs			
MOCVD Run #1053				
Cap	GaAs	0.31	p^+	8.0×10^{19}
Window	AlGaAs	0.03	p^+	1.0×10^{18}
Emitter	GaAs	0.5	p^+	2.0×10^{18}
Base	GaAs	3.0	n	8.0×10^{17}
BSF	AlGaAs	1.0	n^+	2.0×10^{18}
Buffer	GaAs	1.0	n^+	2.0×10^{18}
Substrate	GaAs			

counts (annihilation events) are collected with a count rate of 2 kHz. The change in lineshape of the annihilation energy distribution has been calculated using the standard Doppler S-parameter [23], which is defined as the number of counts in some fixed central energy window divided by the total number of counts in the energy spectrum.

A Biorad Polaron PN4200 electrochemical profiler has been used in conjunction with a Polaron PN 4250 SPV attachment to study the defect nonuniformity from the surface through the p-n junction interface. A detailed description on the operation of the depth-resolved SPV technique is to be published elsewhere [25]. By collecting SPV spectra taken at different etch depths, comparative ratios of one SPV spectrum divided throughout the wavelength scan yield information about the presence of localized defect regions in the emitter and base of the solar cell [25,26].

2.23 SPAS Modeling

The deconvolution of the positron energy dependent (depth dependent) Doppler lineshape parameter, S(E) has been premised upon a previously developed multilayer model [22]. Each layer is assumed to be homogeneous and well-defined, therefore possesing a characteristic lineshape parameter S_i, where i is the layer dependent upon the layer material, deposition conditions, and dopant density. S(E) is defined as the superposition of S_i weighted by the probability, $g(E)_i$, that positrons of energy E will annihilate in layer i such that

$$S(E) = \sum_i g(E)_i * S_i \qquad (1)$$

where

$$g(E)_i = \int_{a_i}^{b_i} P(z,E)dz \qquad (2)$$

and P(z,E) is the positron implantation profile integrated over the boundaries of the layer i from a_i to b_i. The mean positron implantation depth is functionally dependent upon the material mass density and two material Gaussian fitting parameters. As yet, no detailed experimental investigation has been performed to determine the best Gaussian fitting parameters for each of the MOCVD-grown layers. These parameters were chosen to best approximate the general S(E) behavior and are within the range of previous SPAS studies (although on different materials).

While the above model is useful in delineating the layer boundaries and the relative layer defectiveness, the effects of material density (positron backscattering), localized trapping (e.g., at interfaces or at defect inclusions), and positron diffusion length have been neglected. In the current analysis, material density effects may be important since the $Al_xGa_{(1-x)}As$ (x = 0.9) is less dense than adjacent GaAs layers. If the AlGaAs layer were sandwiched between two GaAs layers, an apparent enhancement of S_i for the AlGaAs layer relative to the GaAs layers could result.

Differential positron trapping across interfaces has been shown to be important for an SiO_2/Si interface [21] since the positron diffusion length in Si is substantially greater than in SiO_2. As yet, the positron diffusion lengths have not been experimentally measured for the layer materials, thus the current modeling effort fails to explain local minimums and maximums in S(E). However, away from the interfaces, it has been assumed that localized defects may be approximated by the superposition of characteristic defect values, S_a, as exhibited in Figure 10. Nonetheless, competitive trapping

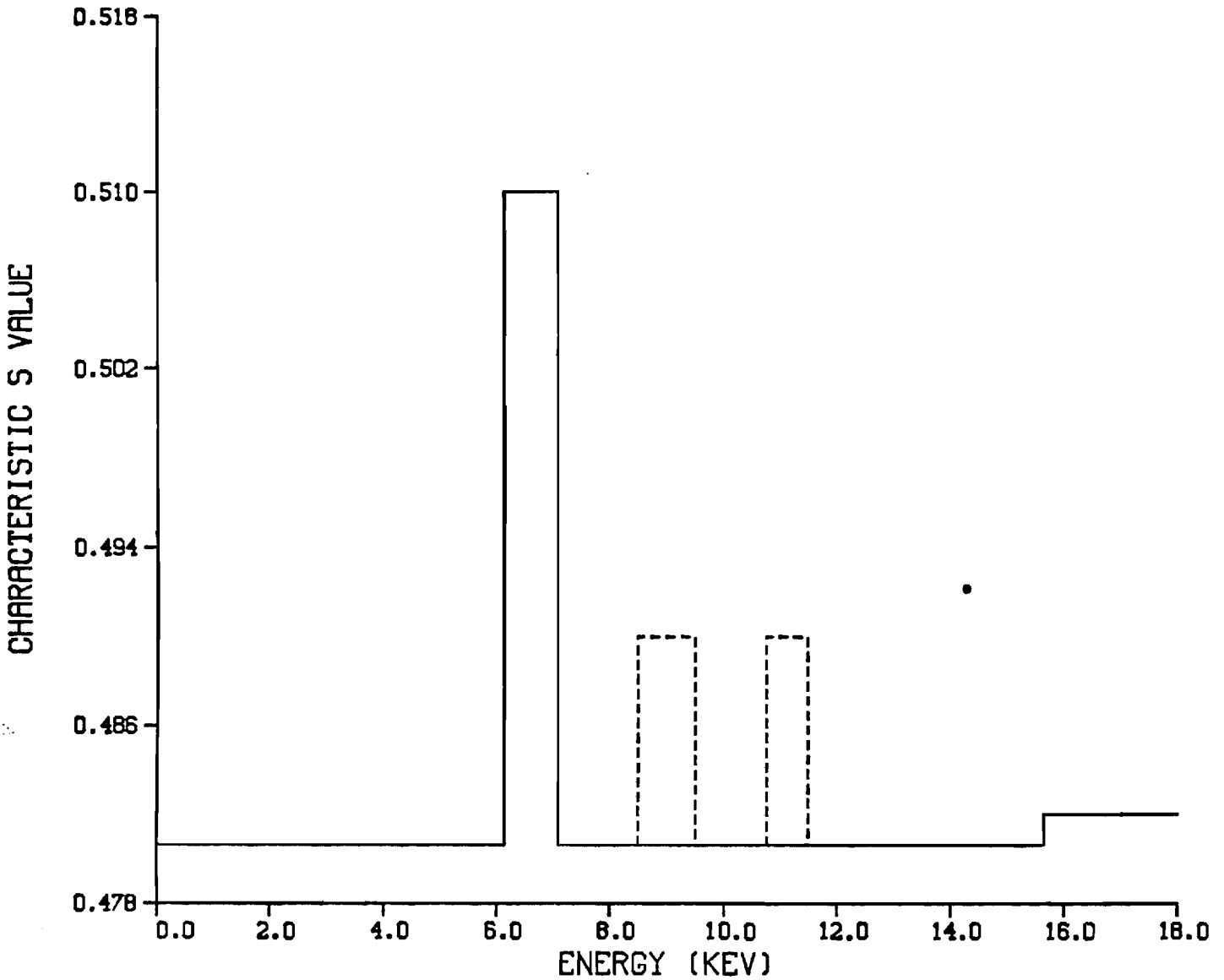

Figure 10. Example of a deconvoluted characteristic lineshape parameter as a function of the material layer for each layer incorporating the superposition of the layer contributions, S_i, (solid lines) and the local defect contributions, S_d (dashed lines).

between localized defects within the layers or between localized defects and nearby interfaces will accentuate the experimental S(E) minimums and maximums, whereas the model approximation has been shown to raise or lower S(E) in a more gradual manner.

2.24 Results and Discussion

Annihilation lineshape measurements have been obtained for the solar cell heterojunctions previously described in Table 2. The variable-energy positron beam has been confined to sampling S(E) spectra with energies of -250 eV to -25 keV which is sufficient to probe through the p-n junction region. Initially, two SPAS S(E) spectra were obtained for two different specimens of MOCVD Run #872 (Figure 11). Both specimens were cut from the same wafer, except that 872A is representative of the center and 872B is representative of the edge. The general features of both specimens are similar; however, two major differences are apparent: (1) the 872B specimen S(E) spectrum is shifted to higher energies with respect to the 872A, and (2) the finer details of the 872A specimen tend to be absent from the 872B specimen.

Before explaining the apparent differences between the two specimens, a number of the features of 872A are first discussed. According to current theoretical model predictions, the depth resolution of the heterojunction layers is as shown in Figure 11. The model predicts that general shape of the convoluted S(E) curve; however, it fails to correctly place the AlGaAs layer and fails to correlate with the finer details of the S(E) spectrum (i.e., the localized minima and maxima). The twin maxima between 5 and 8 keV suggest that positron backscattering may be significant. It is anticipated that the incorporation of backscattering into the theoretical model will shift the

(A)

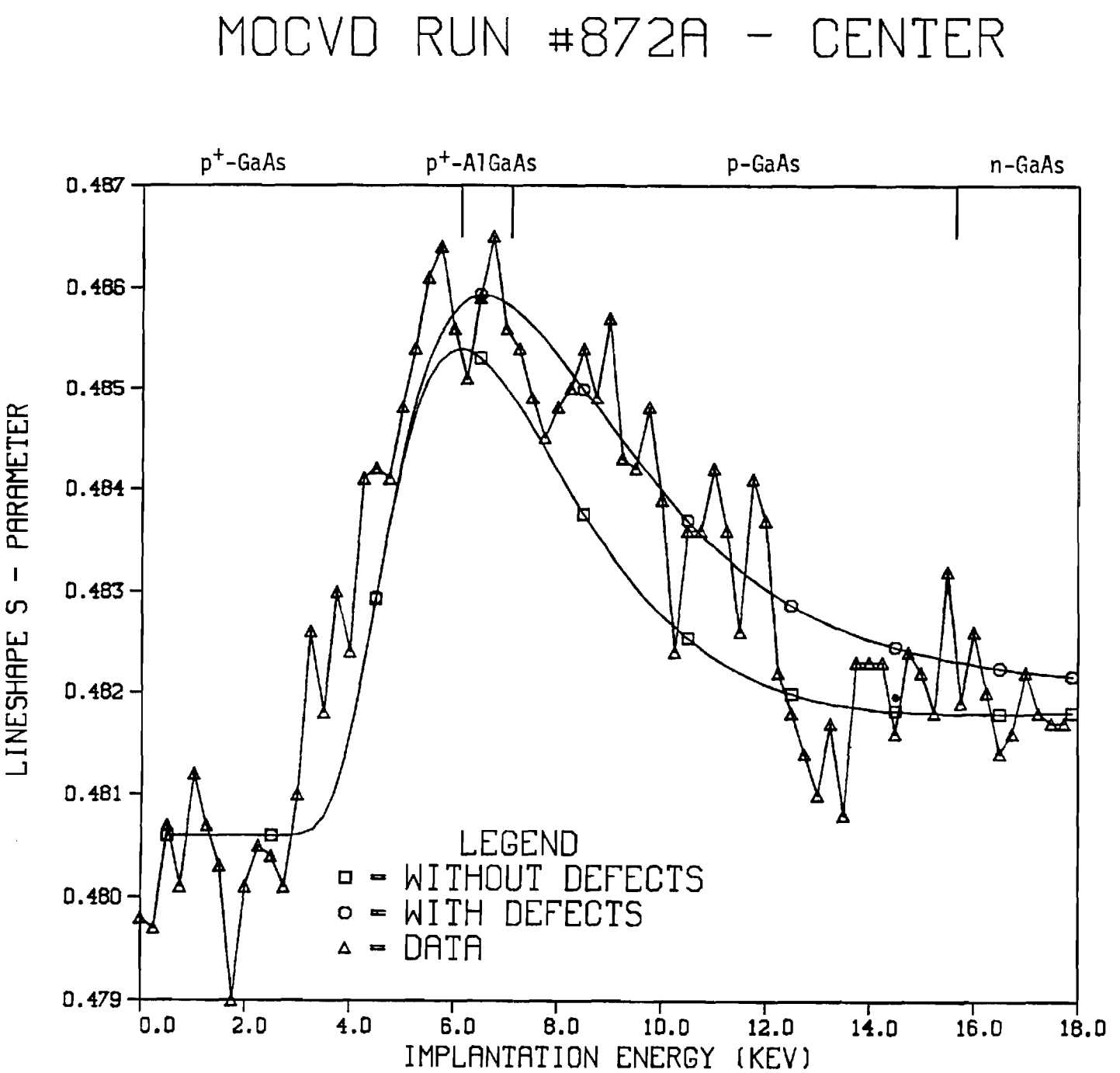

Figure 11.(a) Lineshape parameter, S(E), as a function of incident energy, E, for MOCVD Runs. (a) #872A experimental data connected by triangles. Theoretical approximations to the experimental data (with and without defects) are shown by the smooth solid curves.

(B)

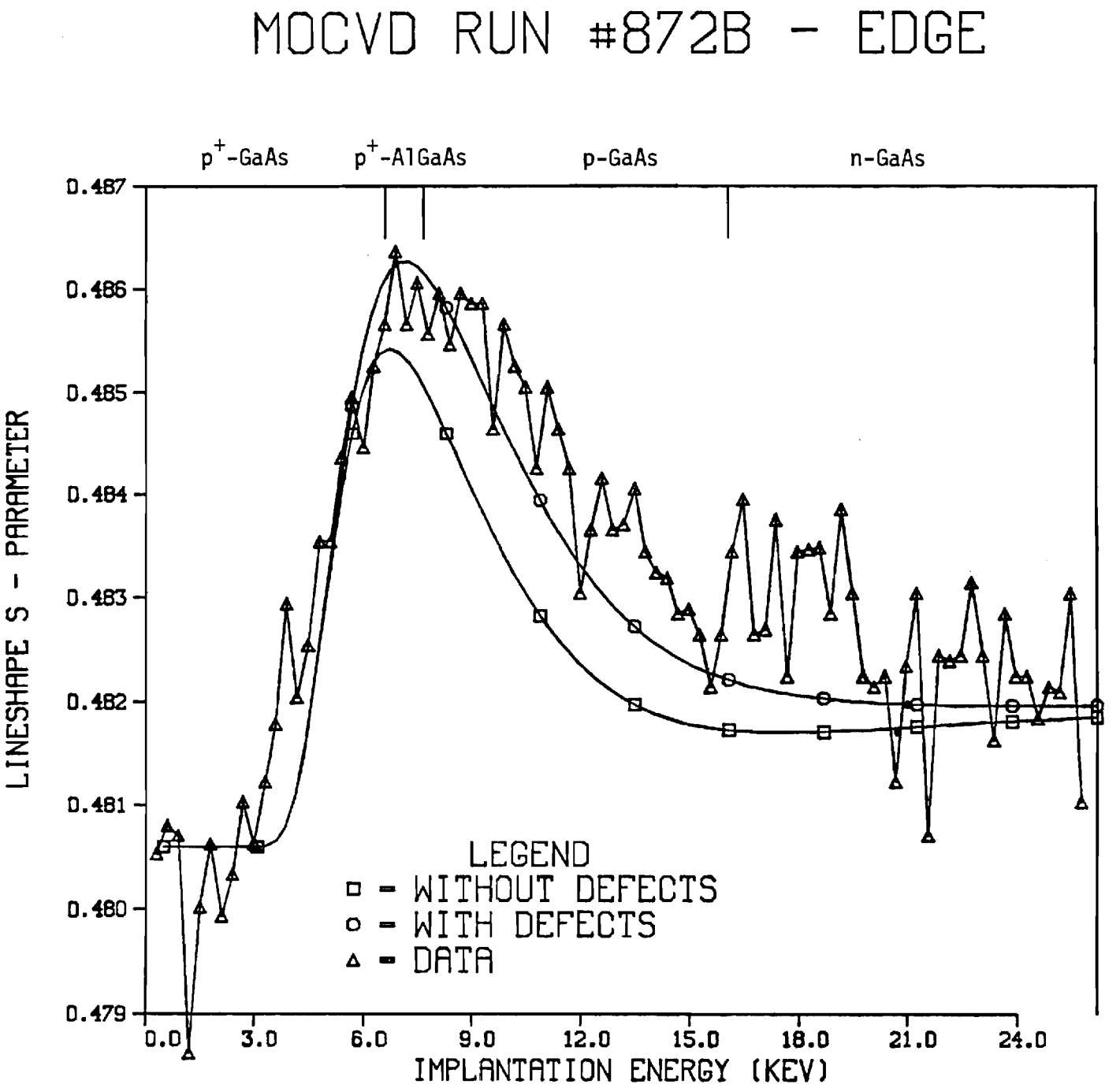

Figure 11.(b) Lineshape parameter, S(E), as a function of incident energy, E, for MOCVD Runs. (b) #872B experimental data connected by triangles. Theoretical approximations to the experimental data (with and without defects) are shown by the smooth solid curves.

predicted position of the AlGaAs layer toward the surface and predict the local maxima near the AlGaAs/GaAs interfaces.

Within the emitter p-GaAs layer, a number of local lineshape maxima exist which have been directly correlated with SPV data. For example, the SPAS data shows a maximum between positron energies of 8.5 keV and 9.5 keV (positron implantation range of .27 to .31 microns). The SPV data clearly shows a defect to exist between .28 and .32 microns (Figure 12). An interpretation of the SPV data is as follows [26]:

(a) the spectra ratio between .22 and .21 microns is indicative of a defective region below the surface in comparison to the material that has just been removed;

(b) the spectra ratio of .28/.22 microns shows that a defective region exists near the surface, but further into the emitter layer, the p-GaAs is less defective;

(c) the spectra ratio of .32/.30 being relatively flat and equal to unity indicates that the defective region has been completely traversed.

When the existence of a local defect region (layer) is incorporated into the model calculation the agreement between the predicted curve and the experimental data is improved. However, the model is still incapable of predicting abrupt changes in S(E). As the synergistic effects of positron diffusion and trapping are folded into the model, it is anticipated that these sharp interfaces will be explained.

Another significant characteristic of the S(E) spectrum is the apparent broad troughs (minima) located between energies 7.5 and 8.5 keV and between energies 12.5 and 14 keV which correspond to the depth ranges of .21 to .27

microns and .50 and .60 microns, respectively. These depth ranges coincide with the AlGaAs/GaAs emitter interface and the p-n junction. Thus, a number of possibilities exist to explain the local minima in S(E). First, a strong electric field is present at the interfaces as a result of band bending. Hence, it is possible that positrons implanted in the space charge depletion region (or within a diffusion length of this region) are swept across the depletion region before an annihilation event is probable. Such an effect would decrease the S-parameter in the proximity of the depletion zone.

Alternatively, the local minimum may be related to the presence or absence of interfacial defect phenomena. In a previous study of SiO_2/Si interfaces [21], it has been shown that differential positron diffusion lengths across an interfacial trap may result in a lower lineshape parameter than either SiO_2 or Si, indicative of higher electron momenta.

Another possible cause of the observed local minimum in the S-parameter may be drawn from the SPV data of Figure 12, where the .22/.21 ratio indicates that the previously etched material (closer to the AlGaAs/GaAs emitter interface) was of superior quality [26].

The explanation for the S(E) spectrum differences between 872A and 872B can be correlated with the MOCVD growth rate difference at the edge of the wafer versus the center of the wafer. It has been observed by Spire [27] that the thicknes of the heterojunction structure is "substantially" greater at the edge, most probably due to a temperature gradient which leads to enhanced nucleation rates at the wafer edge. This effect is sufficient to explain the S(E) spectrum shift of 872B edge specimen in comparison to 872A center specimen. In addition, by increasing the layer thicknesses, higher energy positrons are necessary to penetrate the individual material layers. Thus, loca-

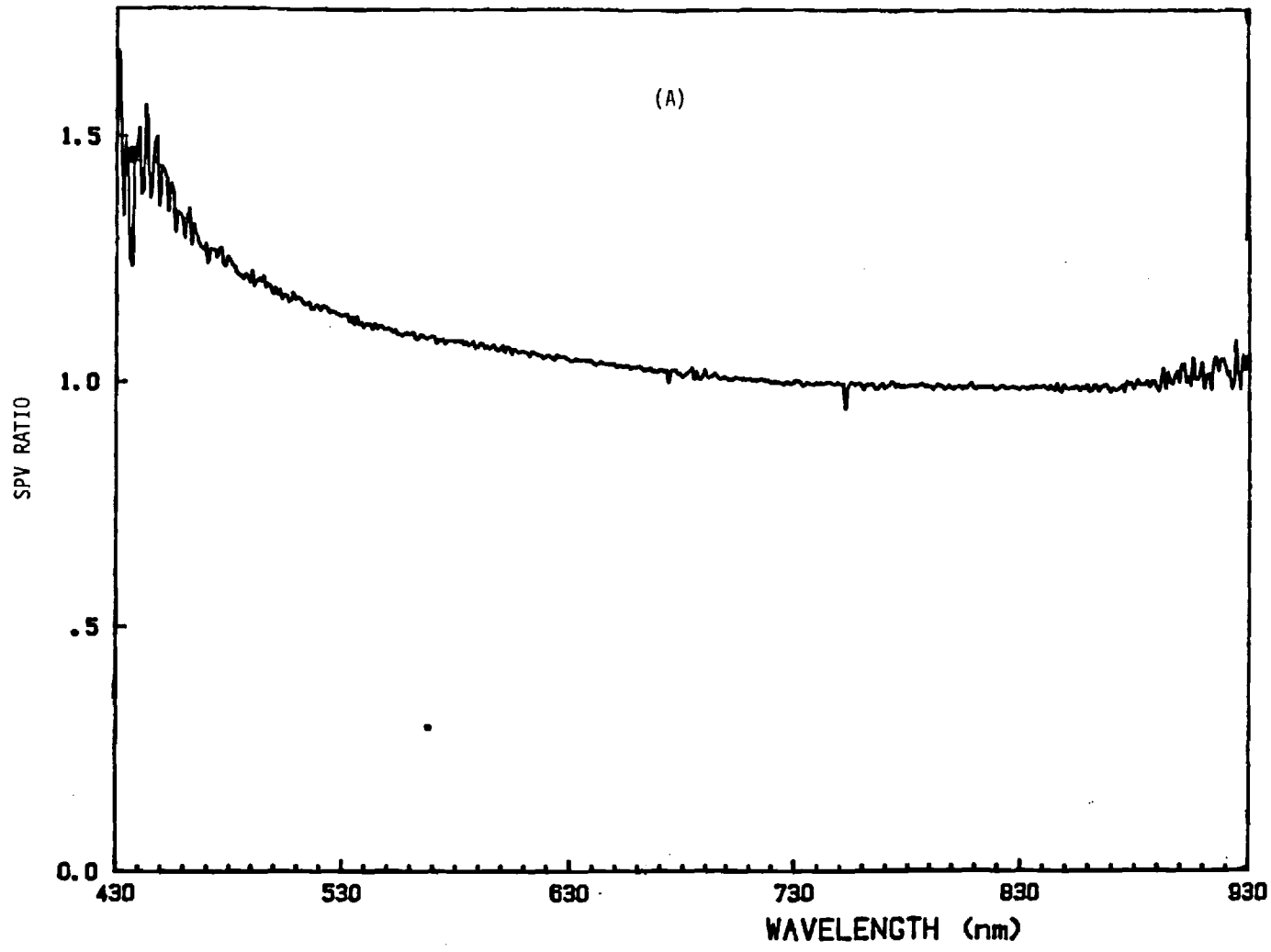

Figure 12.(a) SPV spectrum ratios as a function of wavelength taken at etch depths of (a) .22/.21 microns.

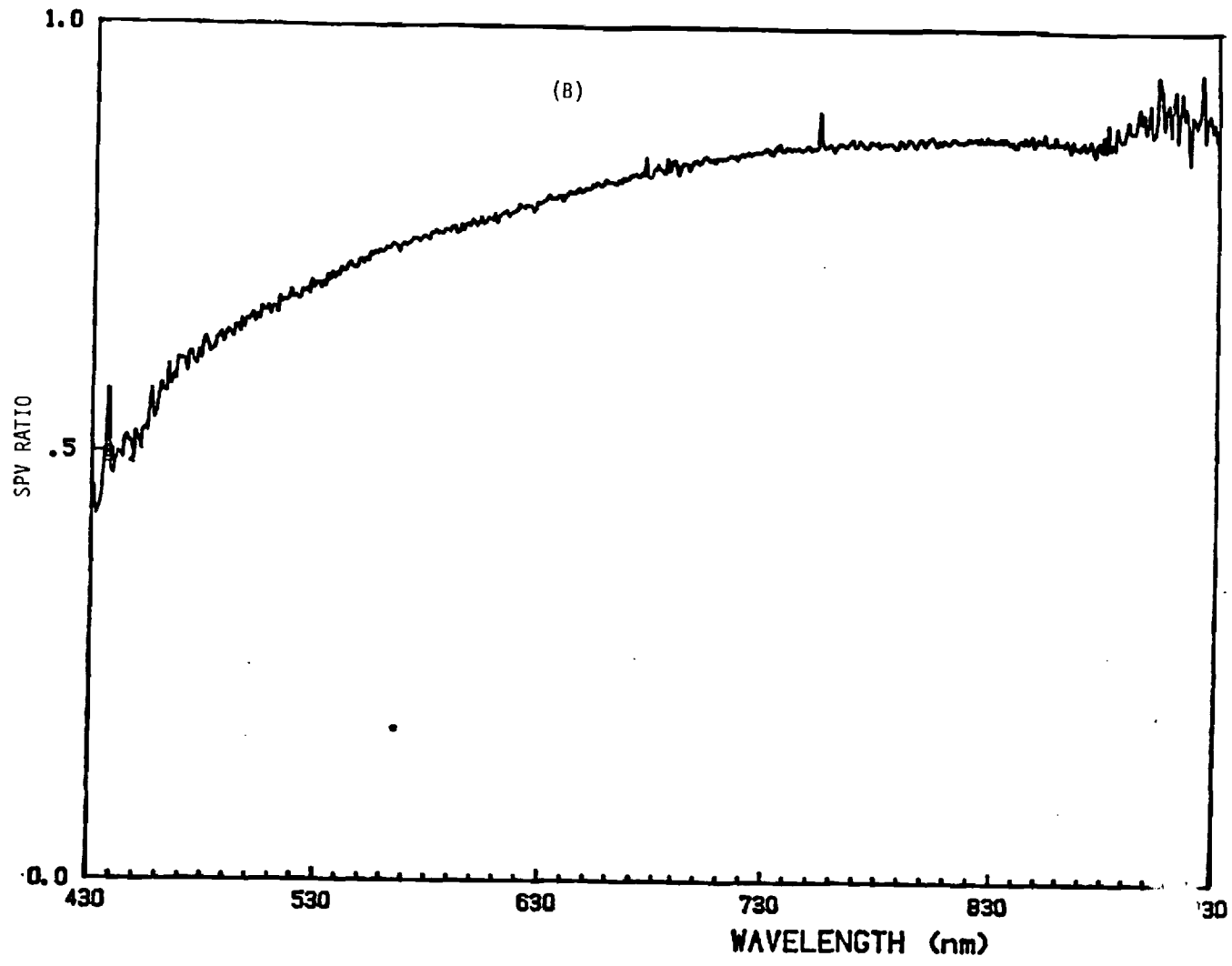

Figure 12.(b) SPV spectrum ratios as a function of wavelength taken at etch depths of (b) .28/.22 microns.

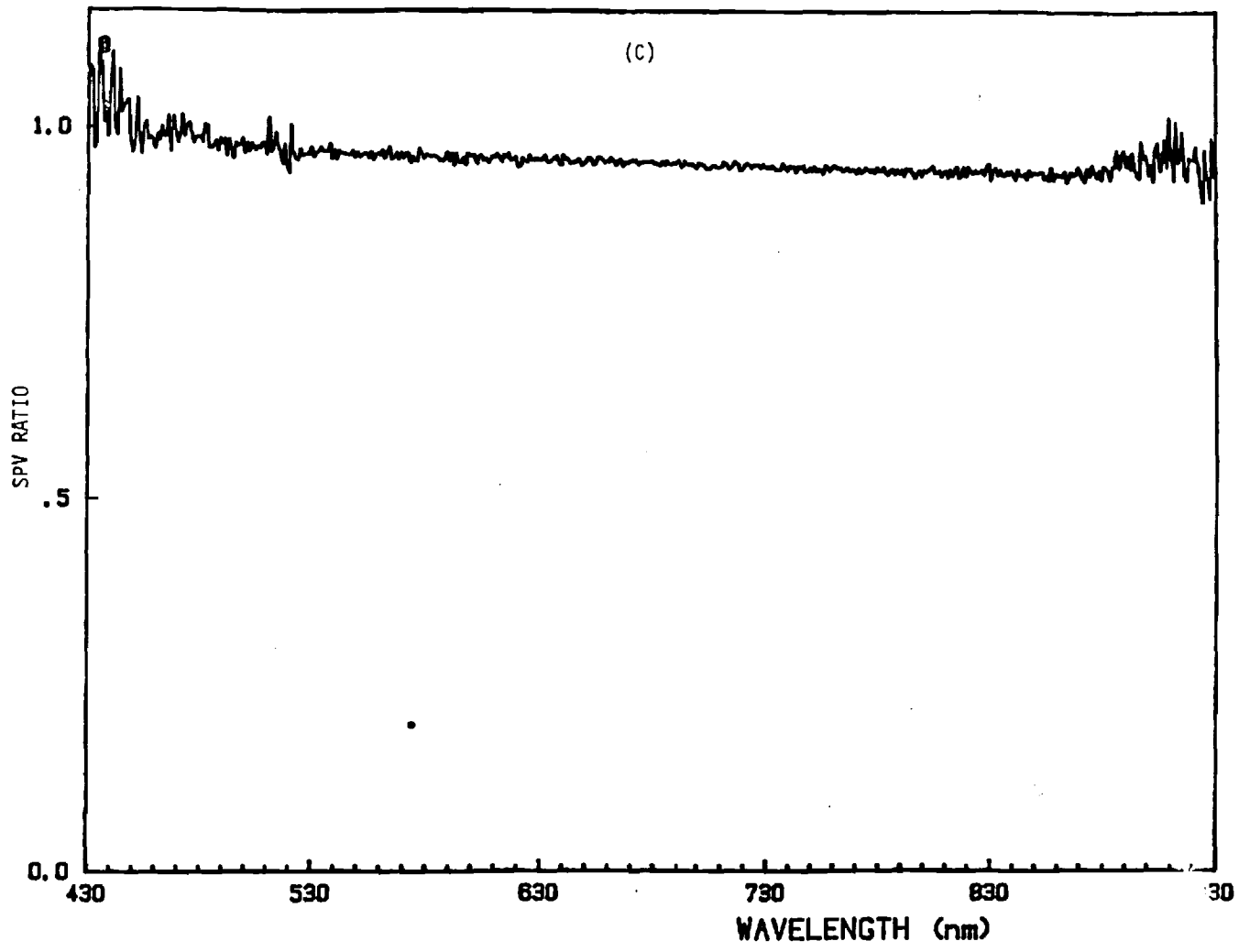

Figure 12(c) SPV spectrum ratios as a function of wavelength taken at etch depths of (c) .32/.28 microns.

lized minima and maxima of the S(E) spectrum should be reduced for 872B in comparison to 872A since the positron stopping profile is approximated by the derivative of a Gaussian function [18]. Another possible result of differential nucleation rates may be enhanced interdiffusion at the interfacial regions between layers, thus broadening the transition region between the heterojunction layers and thereby diminishing the finer details of the S(E) spectrum. SIMS data is currently being obtained in an effort to verify this hypothesis.

Two sets of SPAS data have been taken of MOCVD Run #1053 and subsequently averaged resulting in the S(E) spectrum shown in Figure 13. The 1053 S(E) spectrum is noticeably different from both of the 872 S(E) spectra, and of major significance is the absence of large contrast between the AlGaAs and adjacent GaAs layers. This difference is largely explained by the thicker cap layer, resulting in an AlGaAs window that is translated an additional .157 microns below the surface (see Table 2). The theoretical convoluted S(E) behavior shows a significantly suppressed AlGaAs spectrum for the 1053 specimen when using the identical characteristic S_i parameters of the 872 specimens (Figure 13). However, the model placement of the AlGaAs layer appears to be dubious, and the general experimental features, namely the broad maxima and minima, are not predicted. It is possible that the GaAs cap is thicker than the prescribed dimensions in Table 2, thus translating the predicted positions of the subsequent layers. Auger and ESCA data are currently being obtained to substantiate this hypothesis. If the GaAs cap is .475 microns thick (translation of .175 Angstroms), then the proposed energy positioning of the AlGaAs/GaAs and p-n junction interfaces is as shown in Figure 13. The troughs of 1053 can then be explained in terms of the previous arguments applied to

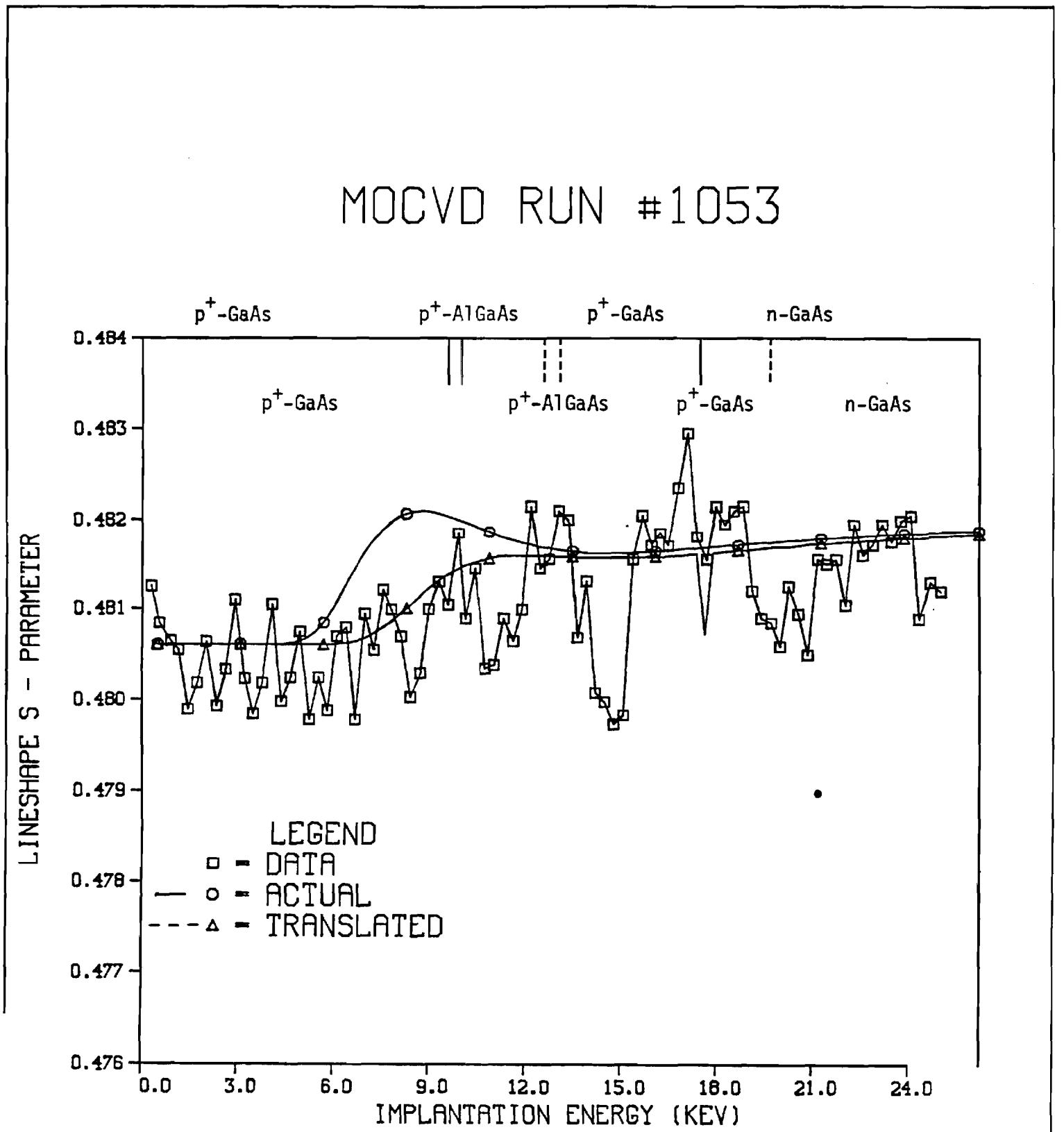

Figure 13. Lineshape parameter, S(E), as a function of incident energy, E, for MOCVD Run #1053 averaged over two profiles of the same specimen.

the 872 specimens: band bending, differential diffusion lengths across an interfacial trap, and the absence of electrically active defects.

2.3 Measurements and Analyses on Additional Device Structures

2.31 LPE-Grown GaAs Heteroface Solar Cells

LPE-grown p^+-n GaAs heteroface solar cell structures were obtained from Hughes Research Labs. The device structure, Figure 14 was mesa etched to provide isolation for electrical characterization. DLTS was successfully performed, identifying a hole trap in the n-GaAs base located 0.57 eV above Ev with a trap density of $3.5 \times 10^{14} cm^{-3}$ as shown in Figure 15. Depth-resolved SPV measurements were attempted but were not successful due to the presence of contact grid and antireflection coating which were not possible to remove without damaging the underlying device structure.

2.32 LPE-Grown AlGaAs Layers on GaAs

Some properties of LPE-grown AlGaAs films on GaAs were studied as a function of Al content. Two target Al mole fractions, 0.20 and 0.38 were used for this study. Figure 16 shows SPV data for each film from which the bandgap values were found to be 1.97 eV and 1.71 eV, correlating well with the desired 0.38 and 0.20 compositions, respectively. The difference in response size can be attributed to both the difference in absorption coefficient (α) since $\alpha \sim (hf - Eg)^{1/2}$, and a smaller diffusion length in the higher bandgap AlGaAs due to a higher degree of alloy scattering. Free carrier effects were not a factor in the SPV variation since the doping profiles of each film were almost identical as determined by the depth-resolved C-V electrochemical profile data in Figure 17.

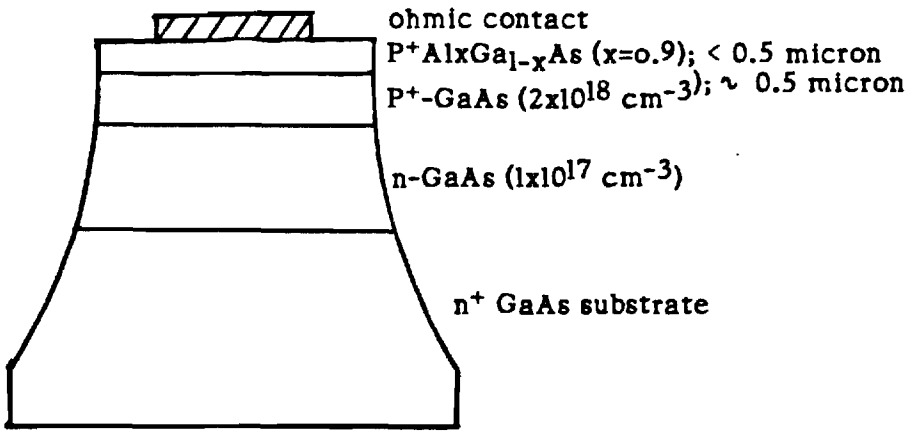

Figure 14. Hughes Mesa Diode Structure used for DLTS Measurements

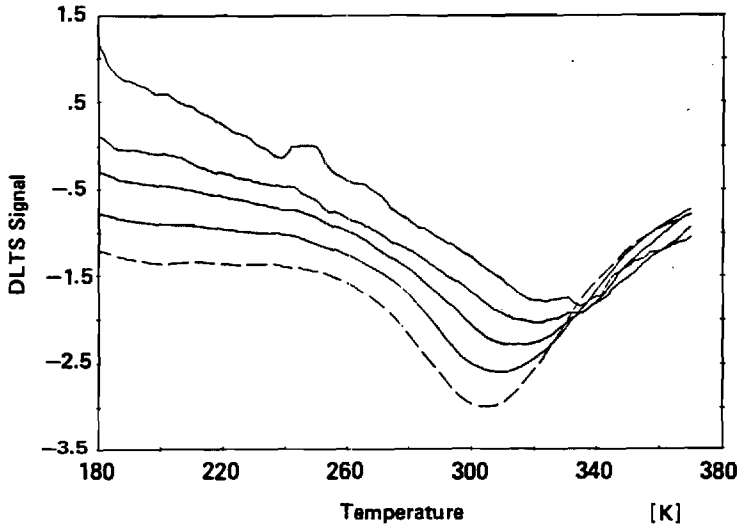

DLTS Spectrum for Hughes Mesa Diode

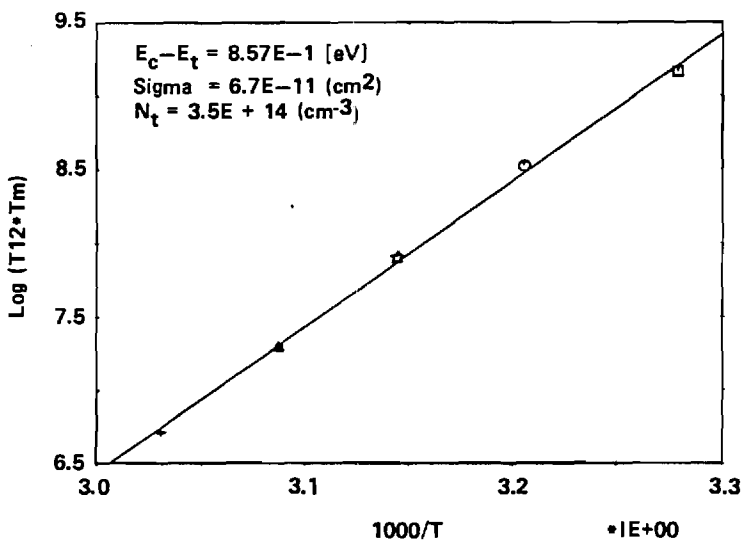

Arrhenius Plot for Deep Level Indicated in DLTS Spectrum

Figure 15. DLTS Spectrum for Hughes Mesa diode (a) and associated Arrhenius Plot (b) for deep level.

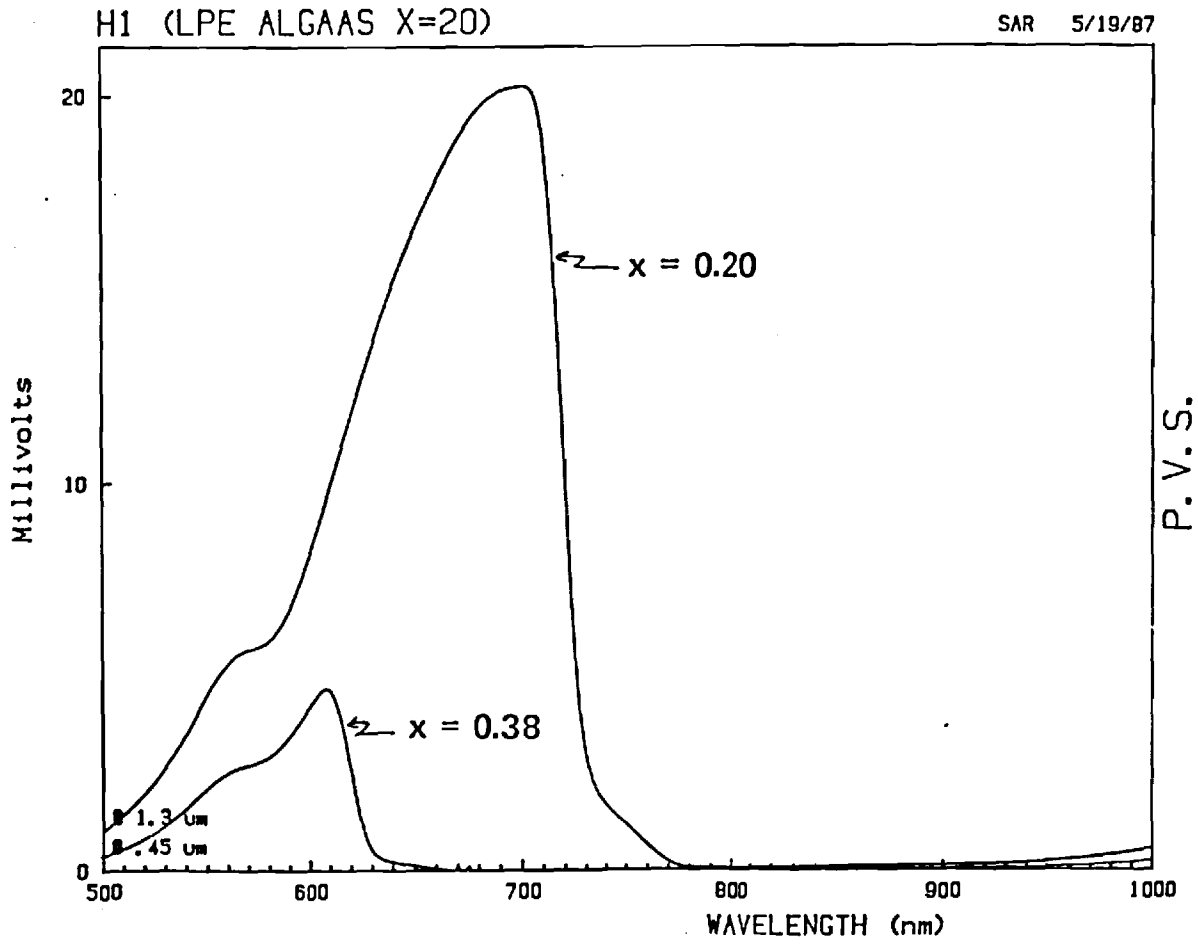

Figure 16. Photovoltage spectra for x = 0.20 and x = 0.38 $Al_xGa_{1-x}As$

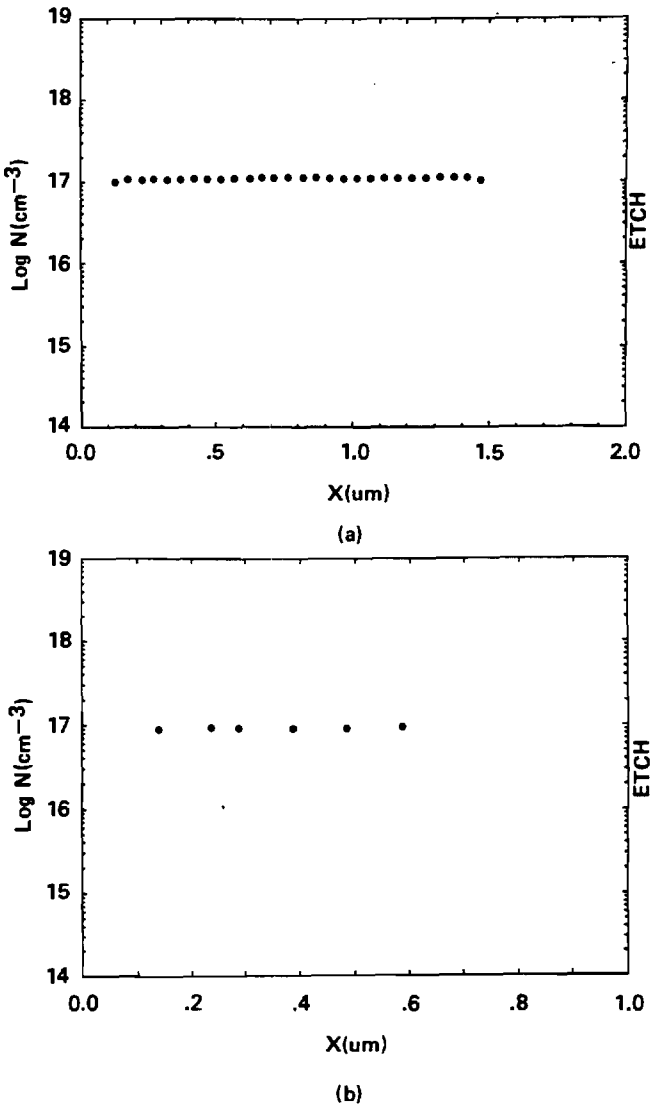

Figure 17. Dopant profiles as determined by the Polaron PN4200 Electrochemical Profiler for a) x = 0.20 and b) x = 0.38 AlGaAs.

3. CONCLUSIONS

A high efficiency, MOCVD grown, GaAs p-n heteroface solar cell has been characterized in order to understand loss mechanisms and optimized its design through extensive computer modeling. Recombination mechanisms were studied using dark I-V, I-V-T, and DLTS measurements which revealed a hole trap at E_v + 0.912 eV for being responsible for the space charge component of the leakage current. Depth-resolved DLTS and SPV measurements were performed to establish that this level was spatially localized near the p-n interface. Although the observed deep level does not effect J_{o1}, it still degrades the cell performance by making the J_{o2} component comparable to the J_{o1} component at the cell operating pont.

Additional defect profiling was accomplished nondestructively using SPAS. It has been shown that SPAS has potential as a profiling tool for high quality epitaxial films and interfaces. The SPAS experimental data provides a profile of distributed material defects that has a strong correlation to SPV results. Also, SPAS appears to possess the capability of performing a three-dimensional characterization of multiple layered structures, as indicated by the differentiation of wafer edge effects resulting from nonuniform film growth temperatures. Finally, SPAS appears to be sensitive to strong localized electric field regions at the AlGaAs/GaAs heterojunctions and the p-n homojunctions.

The internal recombination parameters (lifetime, J_{o1}, FSRV, BSRV) were determined by simulatenously matching the measured and simulated spectral response, J_{01}, and cell data (J_{sc}, V_{oc}, efficiency) with the help of PC-1D and effective recombination velocity models. It was found that a front surface

recombination velocity of 1.25 X 10^5cm/s and a net base lifetime of 8 ns were required to match the cell data. These values were further verified by a good match between the measured and calculated values of J_{o1} using the above FSRV and lifetime profile as inputs to the effective recombination velocity model. This model also gave the emitter and base components of J_{o1} which showed that the base exerted primary control over the leakage current, accounting for ~67% of the total J_{o1}.

Having matched the cell under investigation, guidelines were provided to optimize this structure. For the device studied here, the efficiency can be increased from 21.2% to over 24% by improved front surface passivation (FSRV ~1 X 10^4 cm/s) and base material quality (τ_o = 15 ns). Further efficiency improvement can be realized by thinning the base so that the buffer becomes an active part of the device, forming essentially a two-step base. This structure, however, requires back surface passivation to maximize cell efficiency. This device structure, with a net base lifetime of 20 ns, can result in efficiencies in excess of 25%.

4. REFERENCES

1. R. J. Nelson and R. G. Sobers, "Minority-carrier lifetime and internal quantum efficiency of surface-free GaAs," Appl. Phys., vol. 49, no. 12, pp. 6103-6108, 1978.

2. C. J. Hwang, "Doping dependence of hole lifetime in n-type GaAs," J. Appl. Phys., vol. 42, no. 11, pp. 4408-4413, 1971.

3. R. J. Nelson, "Interfacial recombination in GaAlAs-GaAs heterostructures," J. Vac. Sci. Technol., vol. 15, no. 4, pp. 1475-1477, 1978.

4. P. Dawson and K. Woodbridge, "Effects of prelayers on minority-carrier lifetime in GaAs/AlGaAs double heterostructures grown by molecular beam epitaxy," Appl. Phys. Lett., vol. 45, no. 11, pp. 1227-1229, 1984.

5. J. M. Woodall and J. L. Freeouf, J. Vac. Sci. Technol., vol. 19, p. 794, 1981.

6. P. D. DeMoulin, C. S. Kyono, M. S. Lundstrom, and M. R. Melloch, "Dark I/V characterization of GaAs p.n heteroface cells, Proc. of Nineteenth IEEE Photovoltaic Specialits Conf., pp. 93-97, 1987.

7. P. D. DeMoulin and M. S. Lundstrom, "Theoretical comparison of conventional and unconventional GaAs cell design," Proc. of Nineteenth Photovoltaic Specialists Conf., pp. 925-930, 1987.

8. M. S. Lundstrom, "Device physics of crystalline solar cells," presented at Eight Photovoltaic Advanced Res. Dev. Project Rev. Meeting, Nov. 1987.

9. P. Blood, "Measurement of optical absorption in epitaxial semiconductor layers by a photovoltage method," J. Appl. Phys., vol. 58, no. 6, pp. 2288-2295, 1985.

10. D. K. Schroder, "The concept of generation and recombination lifetimes in semiconductors," IEEE Trans. Electron. Dev., vol. ED-29, no. 8, pp. 1336-1338, 1982.

11. K. W. Loh, D. K. Schroder, R. C. Clarke, A. Rohatgi, and G. W. Eldridge, "Low leakage current GaAs diodes," IEEE Trans. Electron Dev., vol. ED-28, no. 7, pp. 796-800, 1981.

12. A. S. Grove, "Physics and technology of semiconductor devices," Wiley, New York, 1967.

13. D. Rover, P. Basore, and G. Thorson, "Solar cell modeling on personal computers," Conf. Proc. of the Eighteenth Photovoltaic Spec. Conf., Las Vegas, Oct. 1985.

14. C. J. Hwang, Phys. Rev. B., vol. 6, pp. 1355-1359, 1972.

15. A. Haug, "Auger recombination in direct-gap semiconductors: band structure effects," J. Phys. C: Solid State Phys., vol. 16, pp. 4159-4172, 1983.

16. J. S. Blakemore, "Semiconducting and other major properties of gallium arsenide," J. Appl. Phys., vol. 53, no. 10, pp. R123-R181, 1982.

17. A. Rohatgi and P. Rai-Choudhury, "Design, fabrication and analysis of 17-18 percent efficient surface-passivated silicon solar cells," IEEE Trans. Electron Dev., vol. ED-31, no. 5, pp. 596-601, 1984.

18. P. J. Schultz, K. G. Lynn, W. E. Frieze, and A. Vehanen, Phys. Rev. B, 27, 6626, 1983.

19. A. Vehanen, T. Makinen, P. Hautojarvi, H. Huomo, T. Lahtinen, R. M. Nieminen, and S. Valkealhti, Phys. Rev. B, vol. 32, pp. 7561, 1985.

20. K. G. Lynn, D. M. Chen, B. Nielsen, R. Pareja, and S. Myers, Phys. Rev. B, vol. 34, pp. 1449, 1986.

21. A. Vehanen, P. Huttunen, T. Mikenen, and P. Hautojarvi, J. Vac. Sci. Technolo. A, vol. 5, pp. 1142, 1987.

22. B. Nielsen, K. G. Lynn, Y. C. Chen, and D. O. Welch, Appl. Phys. Lett., vol. 51, pp. 1022, 1987.

23. A. Vehanen, K. Saarinen, P. Hautojarvi, and H. Huomo, Phys. Rev. B, vol. 35, pp. 4606, 1987.

24. I. K. MacKenzie, J. A. Eady, and R. R. Gingerich, Phys. Let., vol. 33A, no. 5, pp. 279, 1970.

25. K. G. Lynn, B. Neilsen, and T. H. Quateman, Appl. Phys. Lett., vol. 47, pp. 239, 1985.

26. S. A. Ringel, A. Rohatgi, and S. P. Tobin, in preparation.

27. S. A. Ringel and A. Rohatgi, in preparation.

28. S. P. Tobin, private communication.

5. ACKNOWLEDGEMENTS

The authors would like to thank Steve Tobin of Spire Corporation and Bob Loo of Hughes Research Labs. for their helpful discussions and samples, and Jim Welch of Georgia Tech, MRC, for assistance in the computer modeling, A. B. Dewald and Robert Frost for PAS measurements and analysis, B. Neilson and K. G. Lynn of Brookhaven National Labs for the help in SPAS measurements, and James Gee of Sandia Labs for the valuable discussions and help in arranging the samples.